

Assessing the Material Coherence of Mesoscale Eddies using In Situ Data

Yan Barabinot¹, Sabrina Speich¹, and Xavier J. Carton²

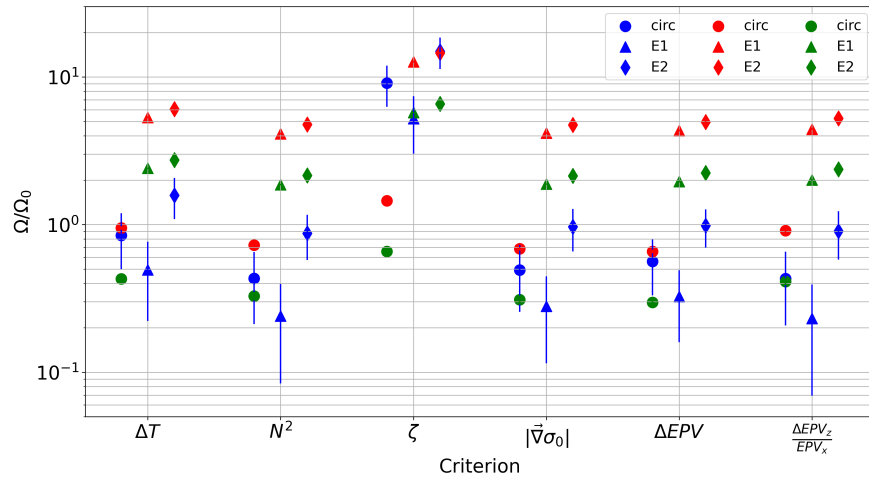
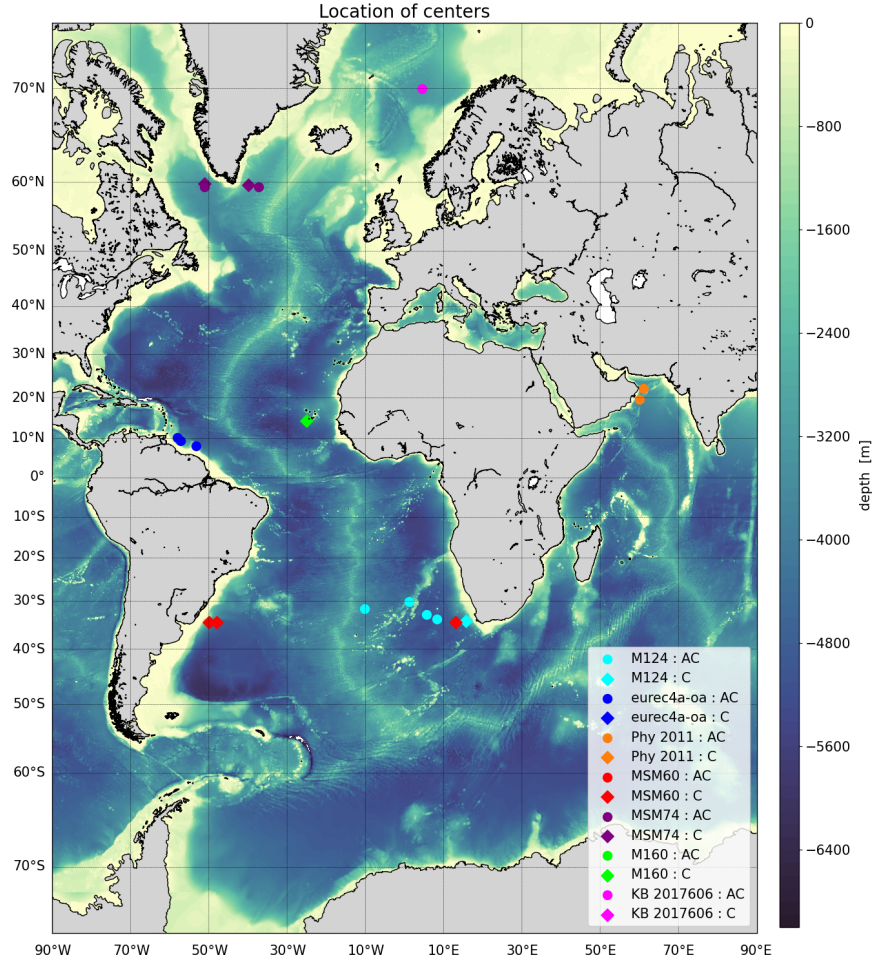
¹Ecole Normale Supérieure

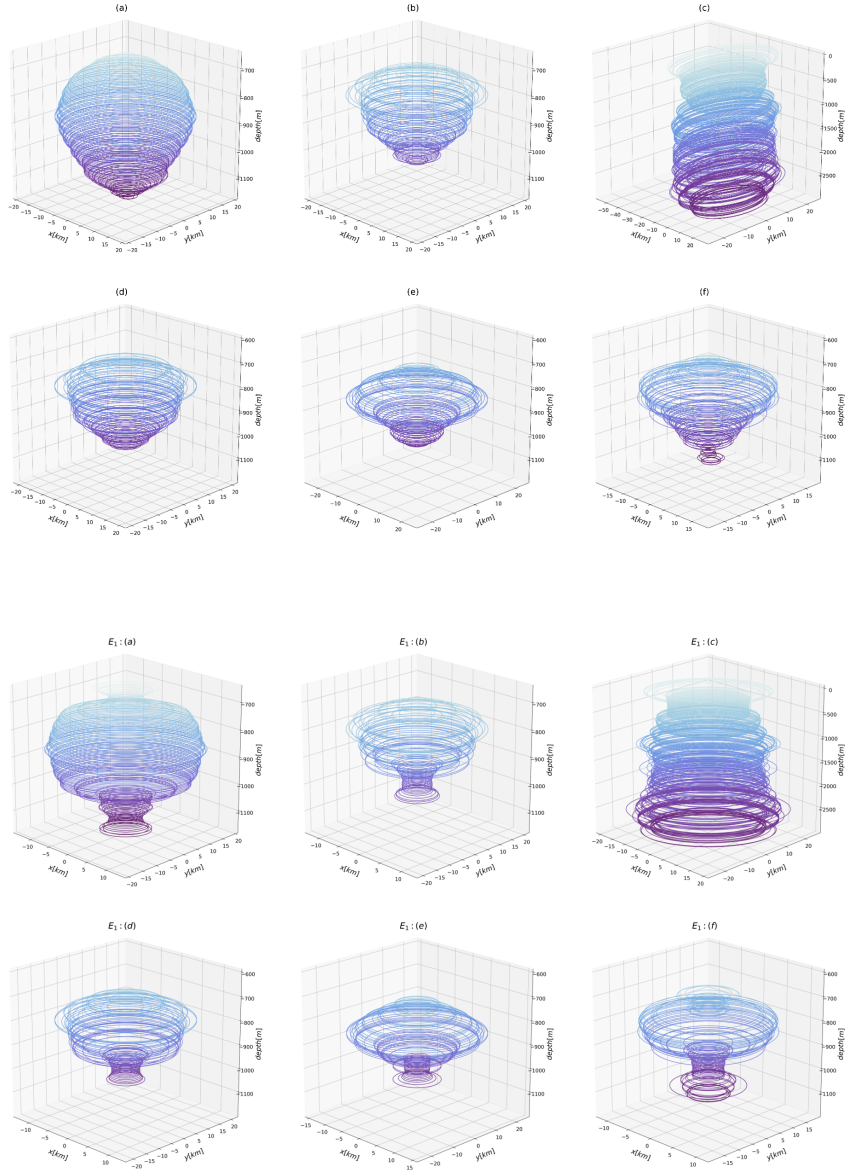
²Université de Bretagne Occidentale

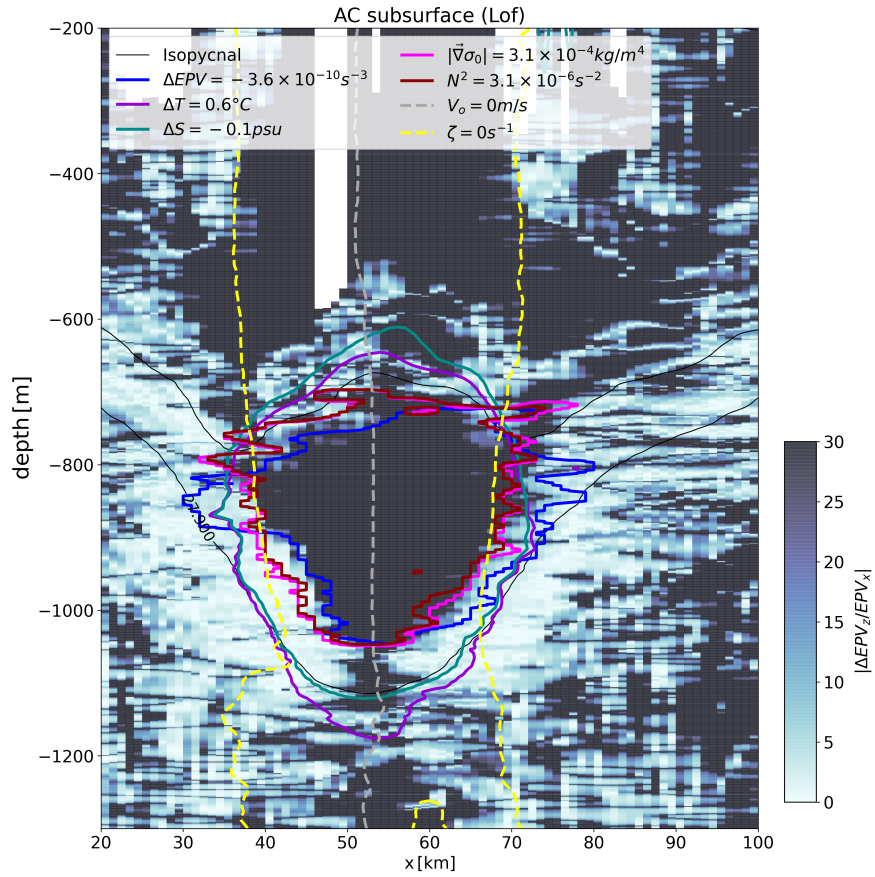
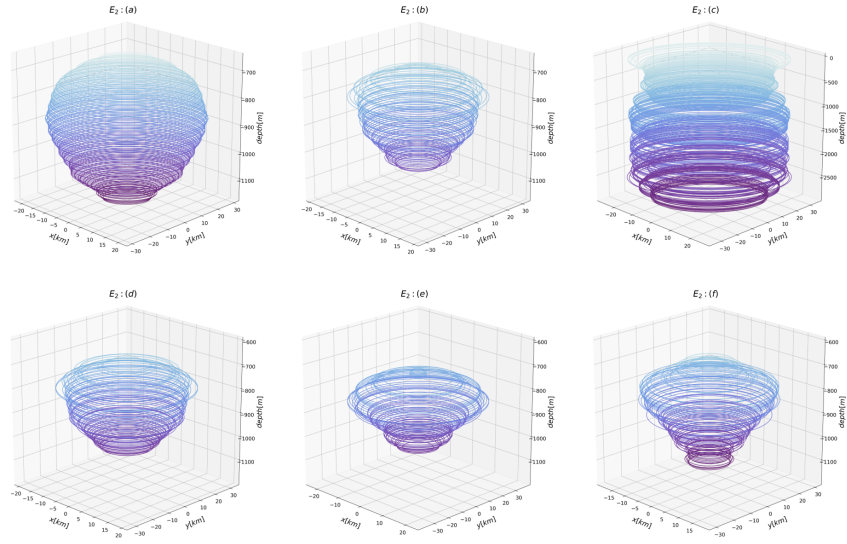
October 26, 2023

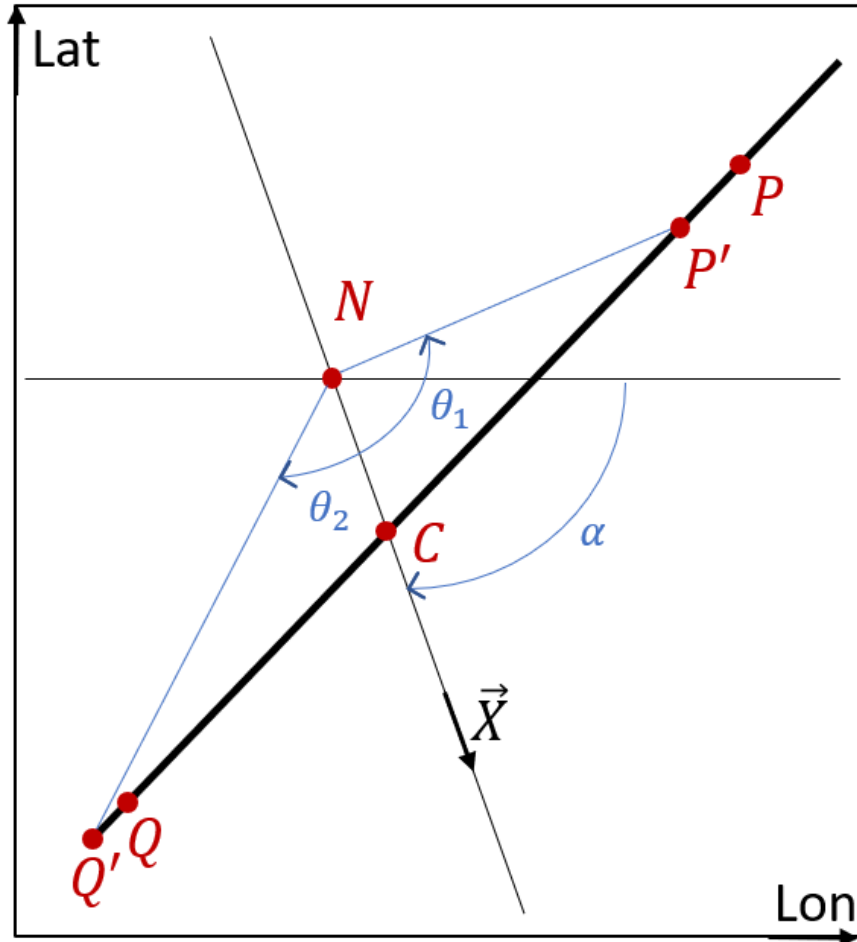
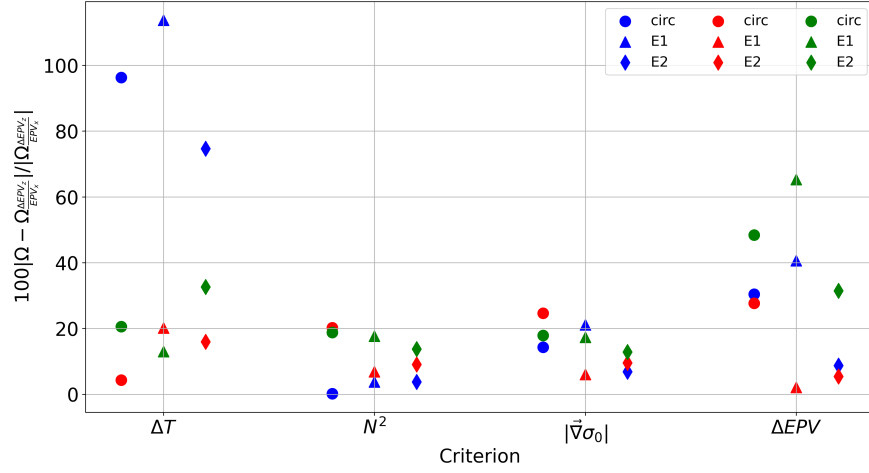
Abstract

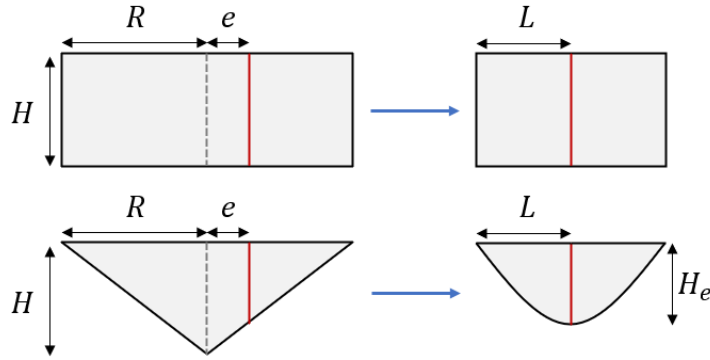
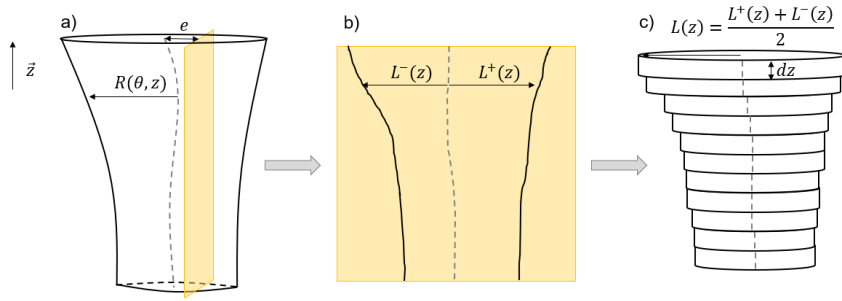
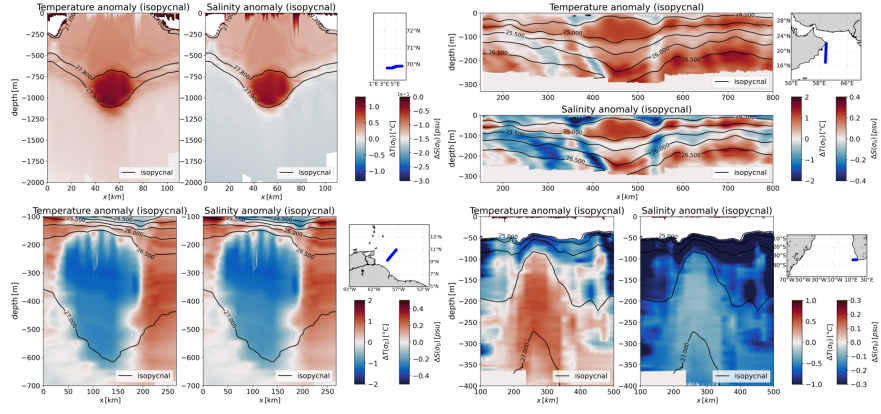
In this paper we analyse the material coherence of oceanic eddies sampled by ships during 9 oceanographic campaigns, 8 of which were conducted in the Atlantic Ocean (EUREC4A-OA, M124, MSM60, MSM74, M160, HM2016611, KB2017606, KB2017618) and one in the Indian Ocean (Physindien 2011). After reviewing previous definitions of coherence, we perform a relative error analysis of our data. To identify the eddy cores and assess the material coherence of the well-sampled eddies (19 out of 28 eddies in total), we use criteria based on active tracers (potential vorticity, temperature, salinity). The maximum tracer anomaly is often below the pycnocline (below the frequency stratification maximum). Therefore, some eddies are not considered to be materially coherent using only surface data, whereas they are when we study their three-dimensional structure. Two methods are then presented to extrapolate eddy volumes from a single ship section. The horizontal and vertical resolutions of the data are critical for this determination. Our results show that the outermost closed contour of the Brunt-Vaisala frequency is a good approximation for the materially coherent eddy core to determine the eddy volume.

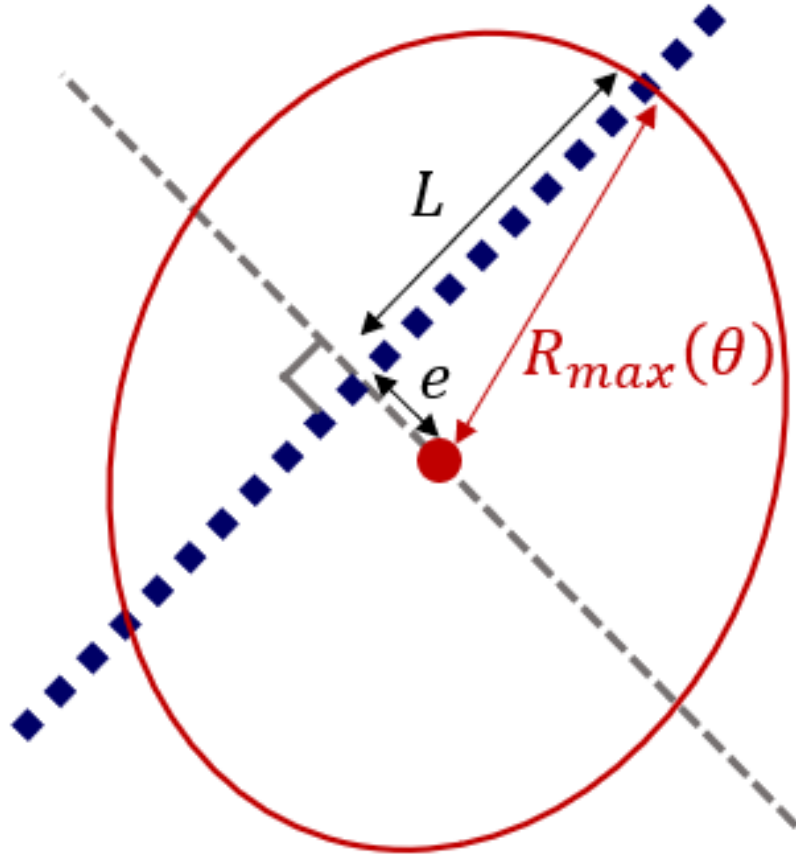












Assessing the Material Coherence of Mesoscale Eddies using In Situ Data

Yan Barabinot¹, Sabrina Speich¹, Xavier Carton²

¹Ecole Normale Supérieure, Laboratoire de Météorologie Dynamique (LMD), 24 rue Lhomond, Paris
75005, France

²Université de Bretagne Occidentale (UBO), Laboratoire d'Océanographie Physique et Spatiale (LOPS),
IUEM, rue Dumont Durville, Plouzané 29280, France

Key Points:

- The material coherence of oceanic eddies sampled by ships during 9 oceanographic campaigns, 8 in the Atlantic Ocean (EUREC4A-OA, M124, MSM60, MSM74, M160, HM2016611, KB2017606, KB2017618) and one in the Indian Ocean (Physindien 2011) is analysed.
- Some eddies are not considered to be materially coherent using only surface data, whereas they are when we study their three-dimensional structure
- The outermost closed contour of the Brunt-Vaisala frequency is a good approximation for the materially coherent eddy core

Abstract

In this paper we analyse the material coherence of oceanic eddies sampled by ships during 9 oceanographic campaigns, 8 of which were conducted in the Atlantic Ocean (EUREC4A-OA, M124, MSM60, MSM74, M160, HM2016611, KB2017606, KB2017618) and one in the Indian Ocean (Physindien 2011). After reviewing previous definitions of coherence, we perform a relative error analysis of our data. To identify the eddy cores and assess the material coherence of the well-sampled eddies (19 out of 28 eddies in total), we use criteria based on active tracers (potential vorticity, temperature, salinity). The maximum tracer anomaly is often below the pycnocline (below the frequency stratification maximum). Therefore, some eddies are not considered to be materially coherent using only surface data, whereas they are when we study their three-dimensional structure. Two methods are then presented to extrapolate eddy volumes from a single ship section. The horizontal and vertical resolutions of the data are critical for this determination. Our results show that the outermost closed contour of the Brunt-Vaisala frequency is a good approximation for the materially coherent eddy core to determine the eddy volume.

Plain Language Summary

Mesoscale eddies are ubiquitous rotating currents in the ocean. They are considered as one of the most important sources of ocean variability because they can live for months and transport and mix heat, salt, and other properties within and between ocean basins. They have been studied extensively from satellite observations because they are often at or near the ocean surface. However, observations of their 3D structure are rare, and calculations of eddy transport are often approximated without precise knowledge of their true vertical extent. Here, we analyse the full 3D structures of mesoscale eddies sampled during 9 oceanographic cruises in order to assess their ability to trap a different water mass from the surrounding. Such eddies are called "materially coherent" and they participate to the total heat and salt transport across basins. However, in this study, we saw that the said "material coherence" depends on the point of view adopted. For instance, mesoscale eddies can be considered as non materially coherent when looking only at the surface whereas they are if we look at depth. As a consequence, in order to evaluate heat and salt transports, future studies must not only base their analyzes on satellite data.

1 Introduction

Mesoscale eddies are ubiquitous energetic structures in the ocean and are one of the major sources of ocean variability (Stammer, 1997; Wunsch, 1999). They are thought to have a major influence on the propagation of hydrological properties by advecting them over long distances and timescales (McWilliams, 1985). The lifetime of such structures often exceeds several months and can reach several years (Laxenaire et al., 2018; Ioannou et al., 2022), highlighting their resilience.

In previous studies, oceanic eddies have been defined in altimetric studies as sea surface height anomalies organised as a set of concentric closed isolines. This set of isolines can be followed in time with a (mostly) continuous trajectory of its centre (Chaigneau et al., 2009; Chelton et al., 2011; Pegliasco et al., 2016; Zhang et al., 2016). As these studies have investigated the persistence of the flow field in time, this characterisation is referred to here as *Kinetic Coherence* (KC). However, KC is only qualitative: in fact, different studies have provided different definitions of the eddy boundary using altimetry data.

For a quantitative characterisation of eddy coherence, oceanographers have relied on flow stability criteria (e.g., Fjörtoft, 1950; Eliassen, 1951; Pedlosky, 1964; Bretherton, 1966; Hoskins, 1974; Carton & McWilliams, 1989; Ripa, 1991). However, recent stud-

ies have shown that even in the presence of moderate, localised instability, a vortex can remain coherent for long periods of time (de Marez et al., 2020). Conversely, stable eddies can be unstable, stretch, shed filaments and disappear under the influence of ambient velocity shear (Carton, 2001; Carton et al., 2010). Therefore, eddy stability is not equivalent to *Kinetic Coherence*.

Nor is KC equivalent to exact eddy invariance: indeed, an eddy can shed filaments or incorporate water masses into its core by lateral diffusion or entrainment. These processes occur at the eddy boundary, where the stress is intense. Conversely, eddy cores are loci of stronger vorticity than strain. Consequently, Eulerian criteria for KC and for the determination of eddy shape have been derived using these two quantities (Hunt et al., 1988; Ōkubo, 1970; Weiss, 1991; Chong et al., 1990; Tabor & Klapper, 1994).

In situ measurements have shown that mesoscale eddy cores contain different water masses from the background. The core water masses are characteristic of the eddy formation region. Mesoscale eddies then transport these water masses over long distances (several thousand kilometres; see (Chelton et al., 2011; Dong & McWilliams, 2007; Zhang et al., 2014). To explain the robustness along the trajectory, Lagrangian approaches have been used to find coherence criteria. Flierl (1981) showed that when the rotational velocity of the vortex is higher than its translational velocity, fluid particles are trapped in the vortex core.

A new theory was then proposed by Haller (2000, 2005); Haller et al. (2015). First, Haller (2005) imposed a vortex coherence criterion to be invariant under a change of reference frame; he criticised the KC theory for being reference frame dependent and not objective. The Lagrangian Coherent Structures (LCS) framework was then used to construct an objective Lagrangian definition of a mesoscale vortex. In Haller’s vision, a coherent eddy traps a mass of water in its core as it forms. This vortex ceases to be coherent when it loses its trapped water mass. We call this definition *Material Coherence* (MC). Objective Lagrangian criteria, such as the LADV method, have been used by these authors to detect materially coherent vortices (Haller, 2015; Xia et al., 2022).

However, these criteria have mostly been validated using altimetry-derived geostrophic velocity fields; these 2D fields are not representative of the wide variety of oceanic eddies. In fact, eddy flow may be partly ageostrophic and not surface intensified. This is also true for eddies identified from satellite altimetry, as the observed sea surface dynamic height provides vertically integrated information about the local density field (e.g., Laxenaire et al., 2019, 2020). Furthermore, MC theory is based only on fluid rotation and does not consider the potential permeability of the eddy boundary due to diffusion processes or lateral intrusion (Joyce, 1977, 1984; Ruddick et al., 2010). Finally, few long-lived MC eddies have been found compared to a larger number of KC eddies (Beron-Vera et al., 2013; Haller, 2015).

The MC definition of eddy coherence is rigorous: it describes how an eddy can trap and transport tracers over long distances. However, the MC view appears to be restrictive because it suggests that mesoscale eddies are too short-lived, whereas their lifetime (assessed independently of altimetry) is consistent with KC theory (Beron-Vera et al., 2013; Laxenaire et al., 2018). Recent studies have shown a difference of more than 30% between the number of KC and MC vortices detected (Vortmeyer-Kley et al., 2019; Liu et al., 2019). This lack of consensus has implications for estimating tracer transport (Dong et al., 2014; Wang et al., 2015; Xia et al., 2022) and hence ocean mixing. The amount of tracer transported by mesoscale eddies appears to be larger using Eulerian criteria than Lagrangian criteria (see Figure 8 of (Beron-Vera et al., 2013)). The estimation of eddy mixing is highly dependent on the criterion used.

It should be noted that the KC and MC definitions do not appear to be incompatible. In fact, altimetry and ARGO floats show that almost all KC eddies are associated

with a thermohaline anomaly in their core. A kinetically coherent eddy can thus be a materially coherent eddy, although it has been defined not by closed trajectories but by closed streamlines. In fact, homogeneous mesoscale eddies (eddies without a thermohaline anomaly in their core) are very rare in the ocean. A few are found in coastal regions, but they are very sensitive to bottom friction and interactions with the topography and are therefore short-lived. The inverse, MC implies KC, is also true, since the definition of MC requires an intense velocity field and kinetic coherence over a long period. Nevertheless, these two definitions, although not exclusive, are obviously not equivalent.

This brief review highlights several questions on which studies should focus: What is the most appropriate definition of eddy coherence in the global ocean? Is a single definition possible? What is the real contribution of eddies to tracer transport? One approach to answering these questions is the concept of potential vorticity. It combines the two aspects of eddy coherence: the existence of closed trajectories within which it remains invariant (in the absence of forcing and mixing), and its strong association with the trapping of water masses (via isopycnal deviations). It is a materially conserved property of eddies. In the ocean, PV mixing occurs at boundaries, either those of the eddy or those of the ocean (surface, bottom, inflows/outflows). Nevertheless, previous studies of PV dynamics have quantified the effects of forcing and mixing processes on the PV distribution (Marshall et al., 1999, 2012). Even though PV is an Eulerian criterion that can vary under changing frameworks, it remains a powerful tool to study ocean dynamics.

In this paper, we provide a first answer to some of these questions, focusing on eddies sampled with relatively good resolution ($O(20\text{km})$ horizontally and $O(10\text{m})$ vertically) during cruises in nine different regions. The aim is to characterise the 3D structure of the sampled eddies in order to assess their material coherence. In fact, only the spatial coherence of mesoscale eddies is accessible with *in situ* data. This spatial coherence can be defined by the convexity of the eddy core volume and thus by its spatial delimitation by the frontal region (Peliz et al., 2014; Barabinot et al., 2023). Therefore, material coherence is only assessed at a given time. For these materially coherent eddies, we propose two methods to extrapolate their volume using a single ship section, and we compare several criteria to draw their core boundaries.

The paper is organised as follows. Section 2 describes the set of *in situ* data used and the identification of the eddies. Section 3 presents the diagnostics used to characterise the core and boundary of mesoscale eddies and links them to MC definitions. In particular, an entire section is devoted to uncertainties that have a real impact on the fidelity of the results. Then, assuming the circularity or ellipticity of a sampled vortex, two methods are proposed to reconstruct its 3D structure. In section 4 we discuss the material coherence of sampled eddies and in section 5 we present results on volume approximations.

2 Data collection and processing

2.1 Data collection: cruises

The data analysed here were provided by 9 oceanographic cruises in 7 different parts of the world: the EUREC⁴A-OA campaign along the north coast of Brazil, which studied mesoscale eddies and the ocean-atmosphere coupling; the MARIA S. MERIAN MSM60 expedition, which was the first basin-wide section across the South Atlantic following the SAMBA/SAMOC line at 34°30'S; the PHYSINDIEN 2011 experiment along the Omani coast (western Arabian Sea), which studied the eddy field in this area; the FS METEOR M124 expedition, which was the first of the two SACross2016 expeditions; the MSM74 cruise, which was dedicated to determining the intensity of water mass transformation and southward transport of water masses in the boundary current systems off Labrador; the M160 measurements, which contributed to understanding the ocean eddies gener-

167 ated in the Canary Current system; and three cruises - KB 2017606, KB 2017618, HM
 168 2016611 - whose main objective was to study eddy dynamics in the Lofoten Basin. The
 169 aim was to collect a relatively large number of eddies sampled in different regions at dif-
 170 ferent times of their life cycle. To be able to derive our diagnostics from the data, the
 171 campaigns must not only have carried out hydrological measurements, but also veloc-
 172 ity measurements of the whole water column. This requirement significantly reduces the
 173 number of potentially available cruises. The table 1 summarises the basic information
 174 about cruises:

Table 1. Basic information on cruises: date, main ocean basin where the campaign took place, sampling instruments used in this paper (it does not refer to every instrument used during cruises).

Name	date	location	Instruments
EUREC4A-OA	20/01/2022-20/02/2020	North Brazil	CTD/uCTD/XBT/sADCP
MSM60	4/01/2017-1/02/2017	SAMBA/SAMOC line (34°30'S)	CTD/lADCP (38kHz)
PHY11	03/2011	Red sea, Persian Gulf	Seasor/xCTD /VM ADCP (38kHz)
M124	29/02/2016 - 18/03/2016	South Atlantic	uCTD/XBT /lADCP (38kHz)
MSM74	25/05/2018 - 26/06/2018	Labrador Basin	CTD /ADCP (75kHz)
M160	23/09/2019 - 20/12/2019	Canary	CTD / lADCP (75kHz)
HM2016611	26/05/2016 - 15/06/2016	Lofoten Basin	CTD /lADCP (38kHz)
KB2017606	10/03/2017 - 23/03/2017	Lofoten Basin	CTD /lADCP (38kHz)
KB2017618	02/09/2017 - 15/09/2017	Lofoten Basin	CTD /lADCP (38kHz)

175 Here we recall the measurement uncertainties depending on the instrument used.
 176 They will be important for estimating errors in the calculated diagnostics. For the CTD
 177 instrument, temperature and salinity are measured with uncertainties of $\pm 0.002^\circ C$ and
 178 $\pm 0.005psu$ respectively. For the uCTD instrument, the uncertainties are $\pm 0.01^\circ C$ and
 179 $\pm 0.02psu$ for temperature and salinity measurements respectively. And for the ADCP
 180 instrument, the horizontal velocity is typically measured with an uncertainty of $\pm 3cm/s$.

181 2.2 Data processing

182 During oceanographic research cruises, data are often collected along vertical sec-
 183 tions that include vertical profiles. Therefore, we define the resolution of a vertical sec-
 184 tion as the average of all distances between successive profiles in the same section. As
 185 hydrological and velocity instruments do not sample the ocean with the same resolution,
 186 the two types of measurements are distinguished (see Table 2). For example, the hydro-
 187 logical properties of the surface anticyclonic eddy from EUREC4A-OA (denoted $N^\circ 1$
 188 in Table 2) were sampled using CTD/uCTD instruments with a resolution of $3.5km$ hor-
 189 izontally and $1m$ vertically, while its dynamical properties were measured using sADCP
 190 (75kHz) instruments with a resolution of $> 1km$ horizontally and $8m$ vertically.

191 The raw data were calibrated and then interpolated. The interpolation of vertical
 192 profiles sampled at different times had to be done with care to avoid creating artificial
 193 fields. To limit noise, only linear interpolations were performed in the \vec{x} (horizontal) and
 194 \vec{z} (vertical) directions. The typical grid size of the interpolated data is $1km$ horizontally
 195 and $1m$ vertically. The data were then smoothed using a numerical low-pass filter of or-
 196 der 4 (scipy.signal.filt in Python). The choice of cut-offs is subjective and depends on
 197 the scales considered. Here, we are considering mesoscale eddies, so we chose $L_x \geq 10km$
 198 and $L_z \geq 10m$ for the horizontal and vertical length scales where possible. In fact, the

199 cut-off period has to be chosen longer than the sampling resolution of the calibrated data.
 200 The smoothing parameters are summarised in Table 2.

201 2.3 Eddies identification and tracking algorithm

202 On vertical density sections, since the rotational dynamics mainly satisfy the cyclo-
 203 geostrophic equilibrium (Cushman-Roisin, 1994), eddies can be identified by observing
 204 vertical deviations of isopycnals; they are usually accompanied by changes in the sign
 205 of the velocity field orthogonal to the section. In order to analyse the true thermoha-
 206 line anomalies in eddy cores, the ship must have passed close enough to the eddy centre.
 207 In the following we separate such sampled eddies from others. We call R_{max} the radi-
 208 us of maximum velocity if the eddy is axisymmetric and e the distance between the
 209 eddy centre and its orthogonal projection on the ship's track (see figure 1). An eddy is
 210 considered to be well sampled if $e \leq R_{max}/2$. Obviously, eddies are not completely ax-
 211 isymmetric and we adapt the criterion to this case using L as defined in figure 1. Us-
 212 ing the Pythagorean theorem, an eddy is well sampled if the following condition is sat-
 213 isfied $e \leq L/\sqrt{3}$. Table 3 summarises the basic properties of vortices and describes which
 214 vortices are well-sampled.

215 The position of the eddy centre is estimated using the routine of Nencioli et al. (2008)
 216 at the depth of the observed maximum velocity, assuming that the position of the centre
 217 does not vary too much with depth. The routine constructs a rectangular area around
 218 the ship track with a given grid size. Then, for each grid point, the distance-weighted
 219 average of the tangential velocity is computed using each velocity vector measured along
 220 the transect. The centre of the eddy is thus defined as the point where the mean tan-
 221 gential velocity is maximum.

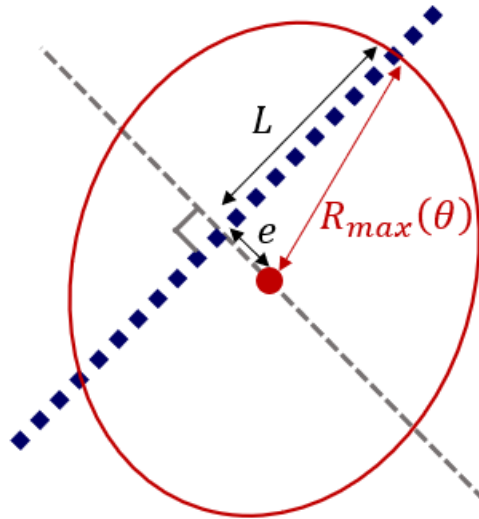


Figure 1. A schematic example of a well-sampled eddy at the sea surface: the red dot indicates the estimated centre; the dark blue squares are locations of vertical profiles; the red circle is the radius of maximum tangential velocity. The dashed grey line is perpendicular to the ship track passing the eddy centre.

222 Finally, we are able to locate every well-sampled eddy during the 9 cruises. The
 223 results are summarised in the map below. In practice, however, some non-well-sampled
 224 eddies have sufficient characteristics to assess their material coherence. In total, 28 ed-

225 dies (20 anticyclonic eddies and 8 cyclonic eddies) were accurately sampled compared
 226 to 19 well-sampled eddies (12 anticyclonic eddies and 7 cyclonic eddies shown in figure
 227 2). Therefore, some biases need to be highlighted: more anticyclonic (AC) eddies were
 228 sampled than cyclonic (C) eddies, the eddies studied come from only 7 specific regions,
 229 which is not representative of all eddies in the global ocean, and of course the eddies were
 230 sampled during their drift, leaving uncertainties in the results. These uncertainties are
 231 discussed in detail in the Methods section.

232 Here we specify the determination of the eddy type. On the one hand, the cyclonic
 233 or anticyclonic aspect is deduced from the deviation of the isopycnals: AC tends to ex-
 234 pand the isopycnals, while C tends to contract them. On the other hand, the surface or
 235 subsurface intensification of the vortex depends on the quantity used to characterise its
 236 vertical structure. In this article, two quantities are used: the location of the maximum
 237 velocity and the location of the maximum thermohaline anomalies (defined by Eqs. (1)
 238 and (2)). A kinetic subsurface eddy (KSub) is defined as an eddy for which the maxi-
 239 mum velocity is below $-70m$ depth. Conversely, Kinetic Surface Eddies (KSurf) are de-
 240 fined. A Thermohaline Subsurface Eddy (TSub) is an eddy for which the maximum of
 241 the thermohaline anomalies on isopycnals (see separate section) is below $-70m$ depth.
 242 Conversely, Thermohaline Surfacic (TSurf) eddies are defined. In fact, ADCP data only
 243 start at a depth of $-50m$ and any processing can be done above this threshold. Further-
 244 more, the lowest value of the climatological mean used to calculate anomalies is some-
 245 times weaker than the lowest value of the *in situ* section. As a result, it is often impos-
 246 sible to calculate anomalies above $-70m$. Therefore, the $-70m$ depth threshold has been
 247 chosen in order to have a unique value regardless of the quantity being considered. In
 248 some cases, eddies are not materially coherent and no maximum of anomalies can be found
 249 at the eddy centre (see part 5.1). Therefore, only the velocity is used to assess the ver-
 250 tical structure. In most cases, if an eddy is labelled KSurf, it will be labelled TSub (same
 251 for Ksub). However, in one interesting case this implication is not true. This will be dis-
 252 cussed later.

253 3 Methods for eddy boundaries characterization

254 3.1 Thermohaline anomalies on isopycnals surfaces

255 The ability of eddies to trap and transport water masses is the basis of the MC def-
 256 inition. Here, we evaluate this definition by computing temperature and salinity anoma-
 257 lies on isopycnals in eddy cores relative to a climatological average following the method
 258 of Laxenaire et al. (2019, 2020). The climatological average of temperature/salinity on
 259 geopotential levels is calculated using ARGO float profiles over 20 years in a small area
 260 around the sampled eddy. The Coriolis dataselection.euro-argo.eu database is used. A
 261 square of side 0.5° is built around the eddy centre estimate, so that the centre is at the
 262 intersection of the diagonals. Taking T^* and S^* as two reference profiles in temperature
 263 and salinity (outside the eddies) and T and S as *in situ* profiles (inside the eddies), ther-
 264 mohaline anomalies on isopycnals are computed as follows:

$$265 \quad \forall \sigma_0, \quad \Delta T(\sigma_0) = T(\sigma_0) - T^*(\sigma_0) \quad (1)$$

$$266 \quad \forall \sigma_0, \quad \Delta S(\sigma_0) = S(\sigma_0) - S^*(\sigma_0) \quad (2)$$

266 where σ_0 is the potential density at atmospheric pressure. These anomalies are computed
 267 on isopycnal surfaces but interpolated to the geopotential level to facilitate comparison
 268 with other criteria. As introduced earlier, we define a thermohaline subsurface eddy (TSub)
 269 as an eddy with an anomaly maximum deeper than $70m$. Conversely, a thermohaline sur-
 270 face eddy (TSurf) has its anomaly maximum above $70m$ depth. These anomalies can sep-
 271 arate two water masses that have the same potential density but different thermohaline
 272 compositions. They are therefore very powerful in delineating the materially coherent
 273 core of an eddy. Taking into account the resolution of the instruments, the uncertainty

Table 2. Cruise names, type and resolution of the 28 mesoscale eddies studied. The resolution of the hydrographic data is denoted by Δ_H , while the velocity data is denoted by Δ_V . For each type of data, the horizontal and vertical resolutions are explained, as well as the cut-off of the low-pass filter used to smooth the data. Some eddies have the same horizontal resolution when sampled along the same transect. The variation in resolution for eddies on the same transect is negligible. AC = anticyclonic eddy, C = cyclonic eddy, surf = Surface eddy, sub = subsurface eddy

N°	Cruise	Type	$\Delta_H x (L_x)$ [km]	$\Delta_H z (L_z)$ [m]	$\Delta_V x (L_x)$ [km]	$\Delta_V z (L_z)$ [m]
1	EUREC4A-OA	AC KSurf/TSurf	3.5 (10)	0.5 (10)	0.3 (10)	8 (10)
2	EUREC4A-OA	AC KSub/TSub	8.4 (10)	0.5 (10)	0.3 (10)	8 (10)
3	EUREC4A-OA	AC KSub/TSub	13 (15)	0.5 (10)	0.3 (10)	8 (10)
4	MSM60	C KSurf/TSub	26.3 (50)	1 (10)	26.3 (50)	8 (10)
5	MSM60	C KSurf/TSub	41.7 (50)	1 (10)	41.7 (50)	8 (10)
6	MSM60	C KSurf	43 (50)	1 (10)	43 (50)	8 (10)
7	PHY11	AC KSurf/TSub	1.8 (10)	0.1 (10)	0.3 (10)	8 (10)
8	PHY11	AC KSub/TSub	1.7 (10)	0.1 (10)	0.3 (10)	8 (10)
9	M124	C KSurf/TSub	25 (30)	0.5 (10)	0.3 (10)	32 (40)
10	M124	AC KSurf/TSub	23 (30)	0.5 (10)	0.3 (10)	32 (40)
11	M124	AC KSurf/TSub	23 (30)	0.5 (10)	0.3 (10)	32 (40)
12	M124	AC KSub/TSub	23 (30)	0.5 (10)	0.3 (10)	32 (40)
13	M124	AC KSub/TSub	12 (30)	0.5 (10)	0.3 (10)	32 (40)
14	M124	AC KSub/TSub	21 (30)	0.5 (10)	0.3 (10)	32 (40)
15	M124	AC KSub/TSub	21 (30)	0.5 (10)	0.3 (10)	32 (40)
16	M124	AC KSub/TSub	20 (30)	0.5 (10)	0.3 (10)	32 (40)
17	M124	AC KSub/TSub	20 (30)	0.5 (10)	0.3 (10)	32 (40)
18	MSM74	AC KSurf/TSub	35.7 (40)	1 (10)	0.3 (10)	8 (10)
19	MSM74	C KSurf/TSub	33.5 (40)	1 (10)	0.3 (10)	8 (10)
20	MSM74	C KSurf/TSub	33.5 (40)	1 (10)	0.3 (10)	8 (10)
21	MSM74	C KSurf	20.3 (30)	1 (10)	0.3 (10)	8 (10)
22	MSM74	AC KSurf	20.3 (30)	1 (10)	0.3 (10)	8 (10)
23	m160	C KSurf	15.1 (20)	1 (10)	0.3 (10)	8 (10)
24	KB2017606	AC KSub/TSub	6.6 (10)	1 (10)	6.6 (10)	8 (10)
25	KB2017606	AC KSurf/TSurf	8.6 (10)	1 (10)	8.6 (10)	8 (10)
26	KB2017606	AC KSub/TSub	5.3 (10)	1 (10)	5.3 (10)	8 (10)
27	HM2016611	AC KSurf/TSurf	8.5 (10)	1 (10)	8.5 (10)	8 (10)
28	HM2016611	AC KSub/TSub	5.8 (10)	1 (10)	5.8 (10)	8 (10)

274 in the thermal (or salinity) anomalies is about $\pm 0.01^\circ C$ ($\pm 0.02psu$) for sections where
 275 uCTD has been used, and $\pm 0.002^\circ C$ ($\pm 0.005psu$) where only CTD measurements have
 276 been made.

277 3.2 Gradients

278 Given (\vec{x}, \vec{z}) as the vertical ship plane, and using smoothed data, derivatives of a
 279 quantity a are approximated by a first-order Taylor expansion as follows $\partial_x a(x+\delta x, z) \approx$
 280 $\frac{a(x+\delta x, z) - a(x, z)}{\delta x}$, $\partial_z a(x, z+\delta z) \approx \frac{a(x, z+\delta z) - a(x, z)}{\delta z}$. Since the Taylor expansion has been

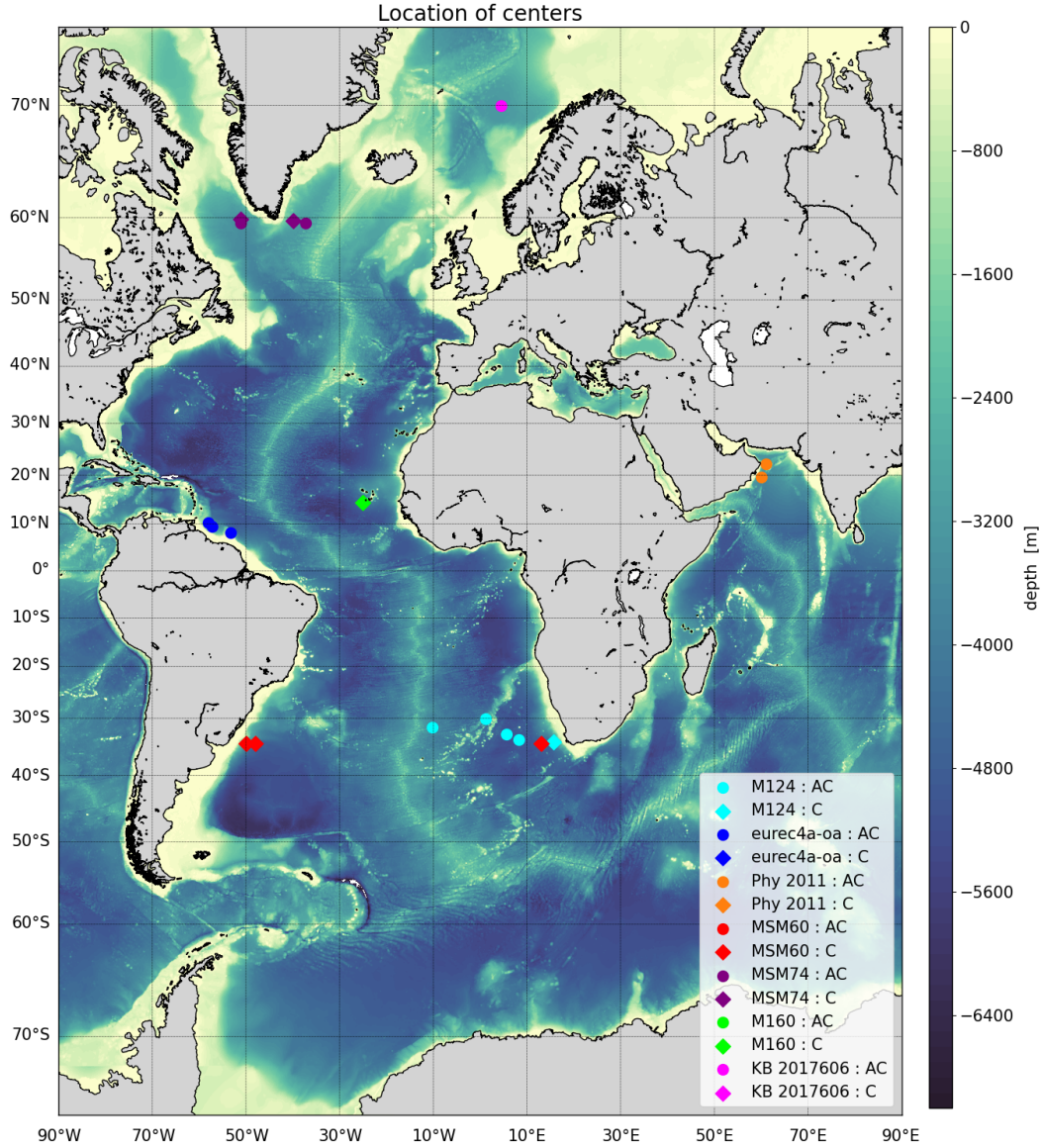


Figure 2. Location of well-sampled eddy centers estimated using the routine of Nencioli et al. (2008)

281 truncated, the terms $(a(x + \Delta x, z) - 2a(x, z) + a(x - \Delta x, z))/\Delta x^2$ and $(a(x, z + \Delta z) -$
 282 $2a(x, z) + a(x, z - \Delta z))/\delta z^2$ of order 2 have been neglected. An approximation of this
 283 term for the temperature, salinity and velocity field has been calculated to support this
 284 idea. Following the approach of Barabinot et al. (2023), second order terms were calcu-
 285 lated and compared with first order terms. For all cruises, the second order terms are
 286 at least 50 times smaller than the first order terms, regardless of the quantity.

287 For a given quantity a , the norm of a gradient in a 2D section is defined as follows:

$$|\vec{\nabla}a| = \sqrt{\left(\frac{\partial a}{\partial x}\right)^2 + \left(\frac{\partial a}{\partial z}\right)^2} \quad (3)$$

Table 3. Basic properties of mesoscale eddies: typical variation of isopycnal deviation (H is an order of magnitude here); radius of maximum velocity on the vertical section ($L \neq R_{max}$ of figure 1); maximum velocity (V_m) associated with L ; apparent Rossby number $R_o = V_m/(f_0L)$. Since mesoscale eddies are not axisymmetric, V_m is taken as the maximum modulus of V_o , the velocity component orthogonal to the ship section. The "Well-sampled" column indicates whether the eddy is well-sampled (Yes) or not (No). The "Complete" column indicates whether the eddy has been completely sampled. The letters [C/B/H] mean [Complete/Boundary/Half]: "Complete" if the eddy structure is clearly visible on vertical sections, a "+" is added if vertical boundaries are visible, "Boundary" if only one boundary is visible and "Half" if one boundary plus the centre is visible. The centre refers to the location where the velocity V_o is zero. If only half of the vortex structure has been sampled, the Nencioli et al. (2008) routine cannot be applied, so we enter "-". In fact, this table underlines the difficulty of obtaining complete (all boundaries visible) well-sampled structures with *in situ* data. For a mesoscale eddy marked "B" in Table 3, the eddy radius cannot be calculated and dashes are used. Note that the radius L has also been estimated for non well-sampled eddies.

N°	Cruise	type	$H[m]$	$L[km]$	$V_m[m/s]$	R_o	Well-sampled	Complete [C/H/B]
1	EUREC4A-OA	AC	70	121	1.14	0.44	Yes	C+
2	EUREC4A-OA	AC	220	71	0.96	0.61	Yes	C+
3	EUREC4A-OA	AC	115	111	0.83	0.32	Yes	C+
4	MSM60	C	375	85	0.6	0.11	Yes	C+
5	MSM60	C	190	42	0.33	0.10	Yes	C
6	MSM60	C	170	28	0.6	0.26	Yes	C
7	PHY11	AC	55	95	0.99	0.38	Yes	C+
8	PHY11	AC	20	10	0.36	0.66	Yes	C+
9	M124	C	120	67	1.53	0.28	Yes	C
10	M124	AC	200	58	1.27	0.26	Yes	H
11	M124	AC	105	55	0.95	0.21	Yes	C
12	M124	AC	-	-	-	-	-	B
13	M124	AC	130	54	0.75	0.19	Yes	C
14	M124	AC	40	34	0.32	0.13	No	C
15	M124	AC	30	52	0.32	0.08	No	C
16	M124	AC	-	-	-	-	-	H
17	M124	AC	150	61	0.73	0.16	Yes	C
18	MSM74	AC	180	28	0.23	0.06	Yes	C
19	MSM74	C	100	35	0.17	0.04	No	C
20	MSM74	C	100	32	0.43	0.1	Yes	C
21	MSM74	C	150	23	0.24	0.04	Yes	C
22	MSM74	AC	150	12	0.3	0.2	Yes	C
23	m160	C	50	49	0.46	0.09	Yes	C
24	KB2017606	AC	-	-	-	-	-	B
25	KB2017606	AC	400	36	0.72	0.14	-	H
26	KB2017606	AC	500	15	0.78	0.34	Yes	C+
27	HM2016611	AC	500	52	0.26	0.04	-	H
28	HM2016611	AC	-	-	-	-	-	B

288 We also defined the Brunt-Väisälä frequency as:

$$N^2 = \frac{-g}{\sigma_0^{(0)}} \frac{\partial \sigma_0}{\partial z} \quad (4)$$

289 where $\sigma_0^{(0)}$ is a reference value, averaged over each profile of the section, and g is the grav-
 290 ity. Since eddies deviate from isopycnal surfaces, they are in fact stratification anoma-
 291 lies. As such, the core appears as a region of low (or high) gradients for AC (or C).

292 To calculate the relative vorticity, derivatives in two different horizontal directions
 293 are required. For a single ship section, this is not possible without further assumptions.
 294 An approximation of the relative vorticity is the "Poor Man's Vorticity" (PMV) intro-
 295 duced by Halle and Pinkel (2003). They decompose the measured velocities into a cross-
 296 track component v_{\perp} and an along-track component v_{\parallel} . The relative vorticity is then ap-
 297 proximated as $\zeta_z \approx 2 \frac{\partial v_{\perp}}{\partial x}$. The factor 2 is added so that the PMV is equal to the ac-
 298 tual ζ in an eddy core with solid body rotation. However, Rudnick (2001); Shcherbina
 299 et al. (2013) used the along track derivative of the cross track velocities without the fac-
 300 tor 2. Both approximations differ only in the way they estimate the cross-track deriva-
 301 tive of the along track velocities. This method can be criticised and other approxima-
 302 tions can be found in the literature. In this article we arbitrarily choose the 2D approx-
 303 imation of Rudnick (2001):

$$\zeta_z \approx \frac{\partial v_{\perp}}{\partial x} \quad (5)$$

304 Unless otherwise stated, the velocity field is always perpendicular to the cutting plane.
 305 Relative vorticity has been used extensively in altimetric studies to compute the eddy
 306 volume. Some Lagrangian criteria such as LADV are also based on this quantity and are
 307 therefore of interest.

308 3.3 Ertel Potential Vorticity (EPV)

309 Here the 3D formula of *EPV* (Ertel, 1942) is simplified and applied to *in situ* data.
 310 Under the Boussinesq approximation and hydrostatic equilibrium, the vertical velocity
 311 vanishes. We denote it as $1/\sigma_0 \approx 1/\sigma_0^{(0)}$. Therefore, following the method of Pierre et
 312 al. (2016), *EPV* for a 2D vertical section takes the following form:

$$EPV = EPV_x + EPV_z = -\frac{\partial V_o}{\partial z} \frac{\partial b}{\partial x} + (\zeta_z + f) \frac{\partial b}{\partial z} \quad (6)$$

313 where $b = -g \frac{\sigma_0}{\sigma_0^{(0)}}$ is the buoyancy, V_o is the velocity component orthogonal to the sec-
 314 tion plane and ζ_z is as defined above. Note that this expression only gives a 2D approx-
 315 imation of the real *EPV* with a baroclinic term EPV_x and a term involving rotating flow
 316 and stretching EPV_z .

317 Therefore, the *EPV* of the ocean at rest (hereafter \overline{EPV}) is

$$\overline{EPV} = f \frac{d\bar{b}}{dz} \quad (7)$$

318 where \bar{b} is the climatological reference profile in the area of the eddy. The *Ertel Poten-*
 319 *tial Vorticity Anomaly* is then calculated on density surfaces (i.e. using density as the
 320 vertical coordinate) as follows:

$$\forall \sigma_0, \quad \Delta EPV(\sigma_0) = EPV_x + \Delta EPV_z \quad (8)$$

$$\Delta EPV_z = EPV_z - \overline{EPV} \quad (9)$$

$$\forall \sigma_0, \quad \Delta EPV(\sigma_0) = EPV(\sigma_0) - \overline{EPV}(\sigma_0) \quad (10)$$

321 As with thermohaline anomalies, this quantity is calculated on isopycnic surfaces
 322 and then represented on geopotential levels. This quantity has been widely used to de-
 323 fine the materially coherent core of eddies and is therefore of interest (Zhang et al., 2014).

324 Following the approach of Barabinot et al. (2023), we also defined the ratio between
 325 the anomaly of the vertical component ΔEPV_z and the horizontal one EPV_x : $\Delta EPV_z/EPV_x$.
 326 In fact, it was shown that the eddy boundary was not locally defined and behaved like
 327 a frontal region subject to instabilities. Consequently, a criterion of the type :

$$\frac{\Delta EPV_z}{EPV_x} > \beta \quad (11)$$

328 with $\beta \sim 30$, this ratio detects the core water that is not in the turbulent frontal
 329 region. This detected water is more stable and is subject to drift with the eddy with-
 330 out being altered by the environment. The value of 30 is chosen so that EPV_x is neglected
 331 before ΔEPV_z and is purely empirical. It follows from the statements of part 5.2.1.

332 3.4 Uncertainties/Relative errors

333 As the gradients are calculated using the finite difference method, the error is easy
 334 to estimate. For example, taking the horizontal gradient of the temperature $\partial_x T$ of a given
 335 velocity profile and resolution, the error is written as follows:

$$\frac{\delta(\partial_x T)}{\partial_x T} = \frac{\delta_H T}{T} + \frac{\delta_H(dx)}{dx} \quad (12)$$

336 where $\delta_H T$ and $\delta_H(dx)$ refer to the uncertainty in temperature and horizontal res-
 337 olution respectively. To obtain an order of magnitude for this error, we can choose the
 338 mean value $T^{(0)}$ for T in the section and the radius of maximum velocity L for the hor-
 339 izontal scale. Here δ_H refers to hydrological data: the horizontal resolution is that of the
 340 hydrological gauges. Similarly, δ_V refers to the uncertainty associated with velocity data.

341 A similar approach can be followed to estimate the errors on gradients of other quan-
 342 tities as well as vertical gradients. For the latter, the typical length scale for z is taken
 343 as the maximum isopycnal deviation with respect to the stratification at rest. As an ex-
 344 ample, we compute the uncertainty in EPV_x . Following the approach we write:

$$\frac{\delta(EPV_x)}{EPV_x} = \frac{\delta_H b}{b} + \frac{\delta_H(dx)}{dx} + \frac{\delta_V V_o}{V_o} + \frac{\delta_V(dz)}{dz} \quad (13)$$

$$\approx \frac{\delta_H b}{b^{(0)}} + \frac{\Delta_H x}{L} + \frac{\delta_V V_o}{V_m} + \frac{\Delta_V z}{H} \quad (14)$$

345 where $\Delta_H x$ is the horizontal resolution of the hydrographic data, $\Delta_V z$ is the ver-
 346 tical resolution of the velocity data (defined in Table 1), $\delta_V V_o$ is the uncertainty in the
 347 velocity measurements, $\delta_H b$ is the uncertainty in the buoyancy. For buoyancy, the lin-
 348 earised equation of state has been used to determine the uncertainty:

$$\delta_H b = -\frac{g}{\sigma_0^{(0)}} \delta \sigma_0 = -\frac{g}{\sigma_0^{(0)}} (-\alpha \delta_H T + \beta \delta_H S) \quad (15)$$

349 where g is gravity, $\sigma_0^{(0)}$ is a reference value taken here as an average over each pro-
 350 file of a considered section, $\alpha = 2 \times 10^{-4} K^{-1}$ and $\beta = 7.4 \times 10^{-4} g/kg$ are classical av-
 351 erages to simplify the calculation. In fact, due to the small uncertainty in the thermal
 352 and salinity fields, the relative uncertainty in the buoyancy $\delta_H b/b$ is often less than 0.1%.

353 Lists of relative errors for the calculated quantities are given in Table 4. In some
 354 cases it appears that the horizontal resolution of the hydrographic data is less than the
 355 radius of maximum velocity provided by the ADCP data, resulting in uncertainties greater
 356 than 100%. This occurs when the distance between two CTD or uCTD profiles is greater

357 than the eddy radius determined using the velocity. It should also be noted that the un-
 358 certainties are driven by the horizontal and vertical resolution of the 2D vertical sections.
 359 In particular, the horizontal resolution of the hydrographic data and the vertical veloc-
 360 ity gradient are shown to be the most critical factors. This is well illustrated by the first
 361 and last columns, where the uncertainty in EPV_x reaches very high values due to the
 362 horizontal buoyancy gradient and the vertical velocity gradient. This can have impor-
 363 tant consequences at the boundary of an eddy where EPV_x increases. On the contrary,
 364 due to the high horizontal resolution of the ADCP data, the uncertainties on the rela-
 365 tive vorticity and EPV_z are limited and mostly remain below 20%.

Table 4. Lists of uncertainties for horizontal and vertical gradients of temperature and salin-
 ity, relative vorticity and both components of Ertel potential vorticity for a 2D vertical section.
 Typical quantities useful in the calculation such as $T^{(0)}$ or $S^{(0)}$ are taken as averages over each
 vertical profile of the vertical section considered.

N°	$\frac{\delta(\partial_x T)}{\partial_x T} [\%]$	$\frac{\delta(\partial_z T)}{\partial_z T} [\%]$	$\frac{\delta(\partial_x S)}{\partial_x S} [\%]$	$\frac{\delta(\partial_z S)}{\partial_z S} [\%]$	$\frac{\delta(\partial_z V_o)}{\partial_z V_o} [\%]$	$\frac{\delta\zeta}{\zeta} [\%]$	$\frac{\delta(EPV_z)}{EPV_z} [\%]$	$\frac{\delta(EPV_x)}{EPV_x} [\%]$
1	2.9	11.5	2.9	11.5	14.1	2.9	3.6	17.0
2	11.9	3.7	11.9	3.7	6.8	3.5	3.8	18.6
3	11.8	7.0	11.8	7.0	10.6	3.9	4.3	22.3
4	31.0	2.7	31.0	2.7	7.7	35.9	36.2	38.6
5	99.3	5.3	99.3	5.3	14.4	108	109	114
6	153.6	5.9	153.9	5.9	10.9	158	159	164
7	1.9	14.6	1.9	14.6	17.6	3.3	3.5	19.5
8	17.0	26.7	17.0	26.7	35	11.3	11.7	52
9	31.1	26.7	31.1	26.7	28.6	2.4	2.8	59.7
10	40.0	16.0	40.0	16.0	18.4	2.9	3.1	58.0
11	41.8	30.5	41.8	30.5	33.6	3.7	4.2	75.5
12	-	-	-	-	-	-	-	-
13	22.1	24.6	22.1	24.6	28.6	4.6	4.9	50.8
14	61.8	80.0	61.8	80.0	89	10.3	11.5	151
15	40.4	107	40.4	107	116	10.0	11.6	156
16	-	-	-	-	-	-	-	-
17	32.8	21.3	32.8	21.3	25.4	4.6	4.9	58.2
18	89.3	4.5	89.3	4.5	17.5	13.4	14.0	106.8
19	95.8	8.0	95.8	8.0	25.6	17.9	18.9	121
20	63.5	8.0	63.5	8.0	15.0	7.3	8.3	78
21	88.3	5.3	88.3	5.3	17.8	12.9	13.6	106
22	125.9	5.3	125.9	5.3	15.3	10.8	11.5	141
23	13.5	16.0	13.5	16.0	22.5	20.0	22.0	36.0
24	-	-	-	-	-	-	-	-
25	14.8	2.0	14.8	2.0	6.2	18.9	19.1	20.9
26	56.7	1.6	56.7	1.6	5.4	60.5	60.7	62.1
27	11.2	1.6	11.2	1.6	13.1	22.7	22.9	24.3
28	-	-	-	-	-	-	-	-

4 Methods to compute eddies volume

There are many methods in the literature to approximate and calculate mesoscale eddy volumes. This step is crucial for estimating tracer transport through these structures. For example, some altimetric studies have used cylinders to approximate eddy cores even when the true vertical structure is unknown. Lagrangian studies are also very powerful to estimate tracer transport using Lagrangian criteria such as LADV (Hadjighasem et al., 2017). However, as mentioned in the introduction, too many of these studies used only altimetric data, which are not suitable to rigorously estimate eddy volumes because they only consider geostrophic surface currents. In fact, there is neither a consensus on the shape of eddies nor a rigorous method to compute their volume. In this section, we describe two reconstruction methods to estimate eddy volumes from a single ship section.

4.1 Basic consideration

Consider an eddy whose boundaries are defined by a criterion (a given isoline of temperature/salinity anomaly, EPV, gradients, etc., see Barabinot et al. (2023)). This eddy has been sampled by a ship transect that does not necessarily cross the exact eddy centre, defined as the location of the null velocity. Therefore, the difference between the exact eddy centre and the centre on the resulting 2D section will affect the reconstruction of the 3D structure and thus the volume.

To illustrate this fact, consider a perfect cylindrical vortex nucleus with radius R and height H . We assume that it is on the surface of the ocean and that it has been sampled by a perfectly vertical ship track as shown in Figure 1, so that L appears as the eddy radius on the 2D vertical section. An estimation by a simple calculation of the eddy volume using this 2D vertical section gives a volume of $\pi L^2 H$, which has to be compared with the real volume of $\pi R^2 H$. Using the Pythagorean theorem, it can be shown that the relative error, expressed as a fraction of the exact volume, is $\frac{e^2}{2R^2}$, assuming $e \ll R$. The relative error is less than 5% if $e \leq \frac{R}{\sqrt{10}} \approx 0.316R$. In this case, e must be less than 31.6% of R for this condition to be true. This condition is not really restrictive and the reconstruction can be quite faithful.

If we now assume that the eddy is cone-shaped with a base of radius R and height H , the relative error is different. Assuming that the eddy has been sampled by a ship track, as in figure 1, the boundary of the eddy will appear as a hyperbola of maximum height H_e on the 2D vertical section. As the eddy will appear less deep than it is in reality, the relative error between the exact and reconstructed volumes will give a more restrictive condition. When the approximated volume is calculated and compared with the real one, the relative error in relation to the exact volume is simply $3\frac{e}{R}$ in first order in e/R . This result follows only from basic geometrical considerations and the method of calculating a volume of revolution (see figure 3). In this case, for the relative error to be less than 5%, e must be less than 1.7% of the eddy radius, which is very restrictive. Adding the horizontal resolution and thus the uncertainty on the radius, the reconstruction method will have a high uncertainty.

Therefore, depending on the eddy shape, the distance between the ship track and the eddy centre e is a critical parameter and strongly influences the uncertainty of the volume approximations. To reduce this uncertainty, volumes are only computed for eddies with a very small value of e . In our database, only 4 eddies ($N^\circ 1, 2, 7, 26$) have been sampled by a ship track with a very small gap ($e < 3km$) and can thus be used to compute volumes.

Different volumes can be studied analytically and the same approach can be followed for subsurface eddies. As shown in previous studies, surface eddy shapes seem to be close to cylindrical or conical volumes (not necessarily with a circular basis), but some

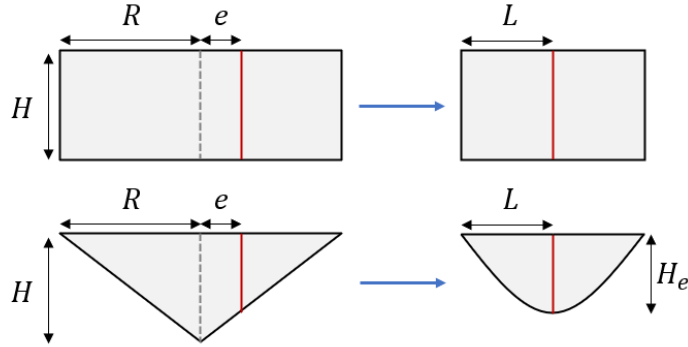


Figure 3. Simple approximation using a ship’s section: an eddy is a solid of revolution (cylindrical shaped above, conical shaped below). On the left is the real eddy core, bounded by a criterion. On the right, the reconstruction based on the ship section. The dashed grey line is the position of the eddy centre, which does not vary, and the red line represents the perfectly vertical section. For clarity, only a 2D view is shown, but each volume is axisymmetric.

416 approximations exist for subsurface eddies. Some of them assimilated eddies to pancakes
 417 because the horizontal scale is much larger than the vertical one (Bars et al., 2011). In
 418 reality, however, an eddy has a more complex shape, depending on the criterion used to
 419 define its boundaries. It is not perfectly axisymmetric and its centre is not perfectly ver-
 420 tical. More precisely, the shape is determined by the rotating flow and depends on the
 421 deformation that the vortex undergoes. It can be stretched and sheared by the mean back-
 422 ground flow. It has been shown that the flow function of the rotating flow can be decom-
 423 posed into azimuthal normal modes (Gent & McWilliams, 1986). Depending on the or-
 424 der of the modes, the flow pattern is modified. When eddies are strongly disturbed, the
 425 decomposition of the flow function into normal modes may include high order terms. In
 426 most cases, however, three modes dominate: order 0, which corresponds to a purely cir-
 427 cular eddy, order 1, which captures the north-south anomaly due to the β effect, and or-
 428 der 2, which corresponds to an elliptical eddy (Carton, 2001; de Marez et al., 2020). In
 429 this context, we propose two approaches to approximate the volume (associated with a
 430 criterion) of an eddy sampled by a ship section, assuming first mode 0 and then mode
 431 2 are dominant.

432 For both approaches, the f -plane approximation is applied. Both reconstructions
 433 are thus performed in a Cartesian space, neglecting the local curvature of the sea sur-
 434 face.

435 4.2 Reconstruction using cylinders with circular base

436 The methodology is illustrated in figure 4. We now reconstruct the 3D structure
 437 of an eddy using the same approach as in figure 3, but we take into account its vertical
 438 tilt. The eddy remains perfectly circular at each geopotential level, its centre being that
 439 given by the ship’s section. The total volume is the sum of the volumes of the elemen-
 440 tary cylinders.

441 This method allows the variation of the eddy radius with depth and the eccentric-
 442 ity of the eddy centre to be conserved. This reconstruction is also relatively straightfor-
 443 ward. However, it assumes that the eddy is perfectly circular at each geopotential level,
 444 which is a strict hypothesis. Also, the centre is that of the 2D ship section and the cal-
 445 culation of the volume does not depend on e , even though we have shown that it has an
 446 influence. To summarise, the approach consists of three steps:

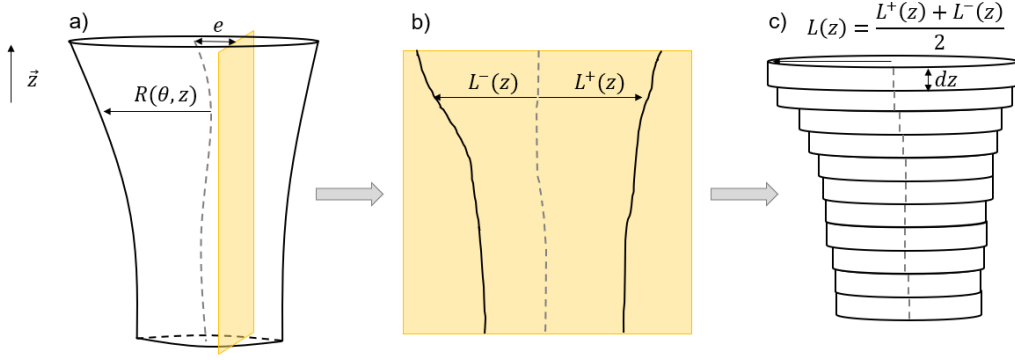


Figure 4. Methodology to reconstruct the 3D structure of an eddy from a single ship track. Here a surface eddy was used, but the approach also works for a subsurface eddy. a) Real surface eddy, for which the volume is defined by a criterion: the real eddy centre is represented by a dashed grey line and the sampled vertical section in yellow. The eddy is not axisymmetric and its radius is a function of the cylindrical variables θ and z . This structure has been sampled by a yellow vertical ship track characterised by the distance e from the real eddy centre. b) Vertical section where the boundary is estimated by the same criterion: here the dashed grey line represents an approximation to the real eddy centre. To be consistent with the previous notation, the radius of the vortex is denoted L . Since the eddy is not symmetric, we differentiate the radius associated with the positive and negative poles of the velocity field (even if the criterion is not based on velocity). c) The 3D shape of the eddy is reconstructed as an association of infinitesimal cylinders of radius averaged between L^+ and L^- and of small height dz . The total volume can be calculated by summation. The centre of each small cylinder is that of the 2D vertical section and thus remains in the plane of the ship section.

- 447 1. Select a criterion (outermost closed contour of a given size) to delimit the mate-
- 448 rially coherent eddy core from its surroundings on the 2D vertical slice.
- 449 2. Compute the position of the apparent eddy centre as the location where the or-
- 450 thogonal velocity V_o is zero and the eddy radius $L(z)$ associated with the selected
- 451 criterion.
- 452 3. Calculate the approximate volume as a sum of elementary cylinders.

453 This method defines the uncertainty due to the resolution:

$$454 \frac{\delta\Omega}{\Omega} = \frac{\int_{-H-\delta(dz)}^0 \pi(L(z) + \delta(dx))^2 dz - \int_{-H}^0 \pi L^2(z) dz}{\int_{-H}^0 \pi L^2(z) dz} \quad (16)$$

454 where Ω is the approximated volume, $\delta(dx)$ is the horizontal resolution and $\delta(dz)$ is the
 455 vertical resolution (depending on the type of device). This formula is valid for a surface
 456 eddy. In the subsurface case, the integral must be replaced by $\int_{-\frac{H+\delta(dz)}{2}}^{\frac{H+\delta(dz)}{2}} \pi L^2(z) dz$.

457 4.3 Reconstruction using cylinders with elliptic base

458 Using altimetry data and detection algorithms, Chen et al. (2019) showed that el-
 459 lipses are the most common shape for ocean surface eddies. Perfectly elliptical eddies
 460 are rare, but ellipses remain the best fit to characterise the shape of almost the entirety
 461 of surfacic eddies. Indeed, isolated eddies tend to be circular, but in the global ocean,
 462 eddies are often deformed by the background flow or their beta drift and thus undergo
 463 elongation. For 20 years (1996-2016), they calculated the best-fit eddy ellipses and anal-

464 ysed the eccentricity of eddies that left an imprint on the ocean surface. They also stud-
 465 ied the averaged orientation of the semi-major axis of these elliptical eddies with respect
 466 to the parallels in each ocean basin. As a result, they obtained the distribution of the
 467 averaged eccentricity as a function of latitude, as well as the distribution of the averaged
 468 orientation of the semi-major axis (see Figure 6 and 8 from Chen et al. (2019)). Although
 469 they worked on surface eddies, we assume that their results also apply to subsurface ed-
 470 dies. Here, we show how to reconstruct an elliptical eddy using the latter two results and
 471 a ship track.

472 The approach is the same as in the previous part. At each geopotential level within
 473 the eddy core, an ellipse is constructed to find an elementary volume of height dz . By
 474 summing at each geopotential level, the total volume is obtained. Figure 5 illustrates the
 475 main geometrical points and constructions useful to find the semi-major and semi-major
 476 axes of the ellipse. For each geopotential level within the eddy core, the main steps can
 477 be described as follows:

- 478 1. Thanks to the orthogonal velocity V_o , the eddy centre C on the ship section is cal-
 479 culated. With a given criterion, the eddy core boundary is determined and P and
 480 Q , the extremities of the core on the ship section, are defined.
- 481 2. Using the Nencioli et al. (2008) routine for the considered geopotential level, the
 482 location of the real eddy centre N can be approximated. N is then the centre of
 483 the ellipse. N is also taken as the centre of the local f -plan Cartesian frame (N, \vec{x}, \vec{y}) ,
 484 where \vec{x} is the zonal vector and \vec{y} is the meridional vector. Starting from N , 1°
 485 north and 1° east are converted into horizontal and vertical length scales.
- 486 3. On this f - plane, the line (NC) can be drawn, and depending on its orientation
 487 with respect to the parallels, we set it as the semi-major axis or the semi-major
 488 axis, following the results of Chen et al. (2019). Since they obtained a global dis-
 489 tribution of the semi-major axis orientation for best-fit eddy ellipses, we can de-
 490 termine which (NC) is more likely. Then P' and Q' , two points on the ship track,
 491 are calculated such that $Q'C = CP'$.
- 492 4. In a 2D Cartesian frame, 5 points are needed to compute the exact equation of
 493 an ellipse. Here, our ellipse is initially constrained by its centre N , the orienta-
 494 tion of the semi-major (or semi-major) axis (NC) , and the eccentricity imposed
 495 by the work of Chen et al. (2019). However, adding the two points P' and Q' will
 496 over-constrain the problem as they are equationed. Therefore, a choice has to be
 497 made between P' and Q' in order to add a unique final constraint. As a conse-
 498 quence, two ellipses can be obtained: one passing through the point P' , arbitrar-
 499 ily called (E_1) , and one passing through the point Q' , arbitrarily called (E_2) . In
 500 the following steps, P' will be used arbitrarily to explain the procedure.
- 501 5. In polar coordinates, if (NC) is the orientation of the semi-major axis, the semi-
 502 minor axis b can be obtained by

$$b = |NP| \sqrt{1 - \varepsilon^2 \cos^2 \theta_1} \quad (17)$$

503 where $|NP| > 0$ is the Cartesian distance between N and P , ε is the imposed
 504 eccentricity and $\theta_1 > 0$. If (NC) is the orientation of the semi-minor axis, we re-
 505 place θ_1 by $\frac{\pi}{2} + \theta_1$. Then we can calculate the semi-major axis a :

$$a = \frac{b}{\sqrt{1 - \varepsilon^2}} \quad (18)$$

506 6. Finally, the ellipse equation reads

$$\left(\frac{x \cos \alpha + y \sin \alpha}{a} \right)^2 + \left(\frac{-x \sin \alpha + y \cos \alpha}{b} \right)^2 = 1 \quad (19)$$

507 where α is defined in the figure 5, x and y are the two variables associated with
 508 the zonal and meridional axes respectively. The approximate volume is: $\Omega = \int_{-H}^0 \pi a(z) b(z) dz$

509 for a surface vortex. For a subsurface vortex the boundary conditions have to be
 510 changed as in the previous part.

511 With this method the uncertainty due to the resolution is defined as:

$$\frac{\delta\Omega}{\Omega} = \frac{\int_{-H-\delta(dz)}^0 \pi(a(z) + \delta(dx))(b(z) + \delta(dx))dz - \int_{-H}^0 \pi a(z)b(z)dz}{\int_{-H}^0 \pi a(z)b(z)dz} \quad (20)$$

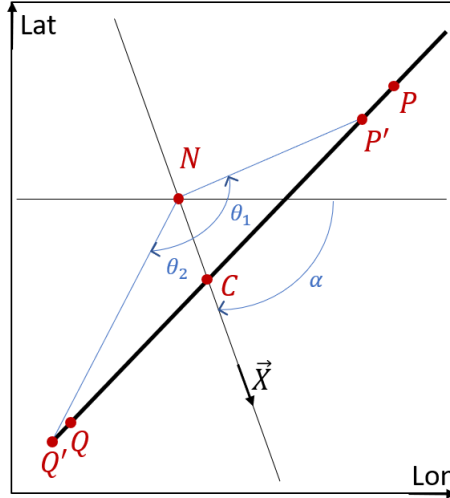


Figure 5. Main geometric constructions for the solution of equations of ellipses.

512 This method allows the non-axisymmetry of the eddy to be maintained and takes
 513 into account the vertical structure. The centre is that of the Nencioli et al. (2008) rou-
 514 tine, which remains an approximation, but it consists in a better hypothesis than for the
 515 previous method. The elliptical shape is more common than the circular shape among
 516 vortices. It should be noted, however, that this method requires that N and C are on
 517 the same semi-major (or minor) axis and that the eccentricity is known. 2 ellipses can
 518 also be determined by this method (no uniqueness). Furthermore, the real upper and
 519 lower limits of the core remain unknown and our method extrapolates in this region. In-
 520 deed, in the ship section, the upper and lower boundaries are characterised by the fact
 521 that P and Q tend to C , so that PQ tends to vanish. However, looking at equation (13),
 522 the semi-major axis will not remain zero when approaching these boundaries. To avoid
 523 this side effect, ellipses are only found at the geopotential level where $PQ \neq 0$. There-
 524 fore the volume will be underestimated.

525 5 Results

526 5.1 Assessing the definition of material coherence with data

527 For each of the mesoscale eddies, thermohaline anomalies on the isopycnals have
 528 been computed using the methodology described in Part 3.1. Examples of anomalies cal-
 529 culated for some eddies are shown in Figure 6. Both salinity and temperature anom-
 530 alies are calculated for each eddy.

531 For the subsurface AC sampled in the Lofoten Basin ($N^\circ 26$ in Table 2), a signif-
 532 icant thermohaline anomaly is visible in the middle of the temperature and salinity pan-
 533 els between $-700m$ and $-1150m$ depth. The location of this anomaly coincides with the

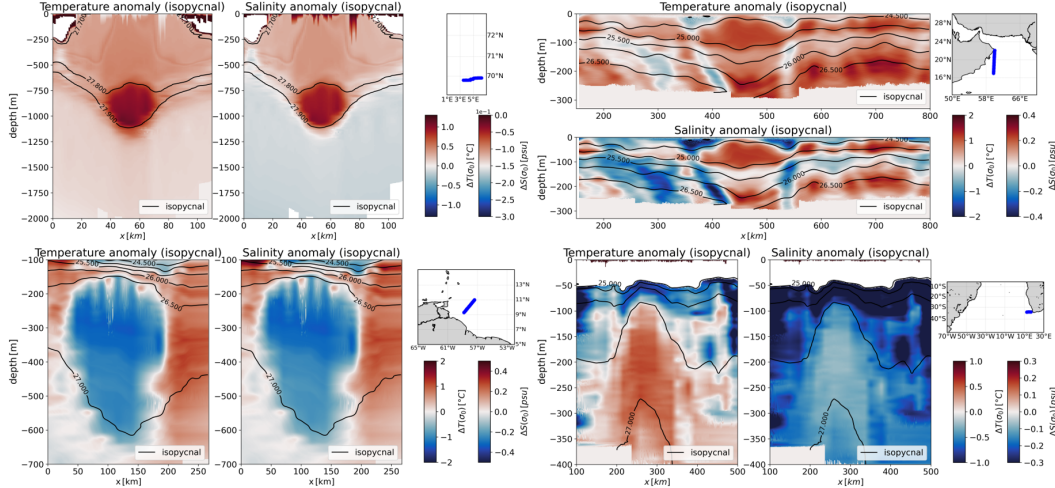


Figure 6. Thermohaline anomalies on isopycnals calculated for mesoscale eddies: the anticyclone in the Lofoten Basin ($N^{\circ}26$), the anticyclone dipole in the Persian Gulf ($N^{\circ}7$), the anticyclone in the North Brazil Current ($N^{\circ}2$) and the cyclone in the southern Cape Basin ($N^{\circ}9$). For each eddy, three panels are shown: both temperature and salinity anomalies and a small map showing the transect (in blue) along which the eddy was sampled. For panels showing anomalies, the abscissa axis is the horizontal scale in km and the ordinate axis is the depth in m . Isopycnals are shown in black. The white bands near the bottom indicate where the data ends. The white regions near the surface illustrate the fact that in some cases the lowest potential density value of the climatological mean is higher than the lowest value of the vertical profiles, anomalies on isopycnals cannot be computed in these regions.

534 maximum isopycnal anomaly, indicating that it corresponds to the eddy core. The trapped
 535 water is warmer and fresher than the climatological average. Compared to the surround-
 536 ing water, the trapped water appears warmer and saltier.

537 A clear negative anomaly can be observed in the vertical sections of the subsur-
 538 face AC sampled during EUREC4A-OA ($N^{\circ}2$). This eddy transports water that is fresher
 539 and colder than the surrounding water. In the case of the surface AC sampled during
 540 Physindien 2011, the warmer and saltier core is located at $x \approx 470km$ and is surrounded
 541 by colder and less salty water that forms a rim around it. The subsurface cyclone sam-
 542 pled during M124 also shows anomalies in the region where the isopycnals show the largest
 543 deviation. Water that is hotter and saltier than its surroundings is trapped in the eddy
 544 core. However, the core is less well localised than in other examples, suggesting either
 545 that the eddy is losing water through instability and filamentation, or that it is not well
 546 resolved in terms of horizontal resolution of vertical thermohaline properties.

547 In the table 5, the maximum values of thermohaline anomalies on isopycnals are
 548 collected for each eddy. The anomalies are calculated with respect to climatological av-
 549 erages. An eddy is considered to be materially coherent when the maximum anomaly
 550 is reached at the eddy centre (region where the velocity tends to zero) and there is a marked
 551 difference in values between the enclosed and surrounding waters.

552 According to the data, 24 out of 28 eddies have a significant thermohaline anomaly
 553 on isopycnals in their core. Thus, 85.7% of the eddies are materially coherent. The abil-
 554 ity to advect a water mass does not seem to depend on eddy size or region. Even eddies
 555 sampled far from their origin showed an anomaly in their core (see Algulhas rings $N^{\circ}15$, 16, 17)).

As the number of eddies studied is small compared to those derived from global satellite altimetry, only hypotheses can be formulated. One can wonder if material coherence is more common than studies based on satellite altimetry have indicated so far.

In our data set, the maximum thermohaline anomaly is often located at depth rather than at the surface, even for eddies detected by satellite altimetry. Indeed, surface thermohaline variability is enhanced by atmospheric forcing. However, this result highlights the limitations of altimetry and surface fields alone for eddy studies. By looking only at the surface, eddy assessments miss what is happening in the subsurface eddy cores. Lagrangian studies suggest that the ability of eddies to trap a water mass is a consequence of closed trajectories. However, such trajectories are not visible at the surface as eddies subduct or form at depth. Therefore, some eddies are not considered to be materially coherent by diagnostics based on satellite altimetry alone, whereas they are by analysis of the entire water column.

Consequently, tracer transport estimates depend critically on how eddies are observed and characterised. Note the proportion of thermohaline subsurface intensified eddies, 60.7%, in our *in situ* dataset. Even if the number of surface intensified eddies is underestimated, because *in situ* measurements often sample the ocean below $-50m$ depth, this ratio emphasises the ubiquity of subsurface eddies and the bias of studies based on altimetry alone, which do not take them into account.

Furthermore, some eddies will appear to be materially incoherent when using altimetry but not when using *in situ* data. In fact, some KSurf eddies (which may have a signature using ADT) have a deep maximum of anomalies and are therefore TSub (see Table 1.). For example, the AC sampled during Physindien 2011, shown in Figure 6, is characterised by a maximum of anomalies at $-90m$, while it was shown by the figure 4 of L'Hégaret et al. (2015) that it is also characterised by an ADT signature. As a result, using only altimetry-based diagnostics, it might not be considered as a materially coherent structure according to Lagrangian criteria, although it is.

In conclusion, in most cases the velocity is correlated with thermohaline anomalies on isopycnals. However, there are a significant number of surface eddies in the velocity field characterised by a deep maximum of anomalies. These eddies increase the uncertainty of tracer transport estimates based on altimetric data alone.

5.2 Volume estimates

5.2.1 3D Eddy Boundary Characterisation

For materially coherent eddies, the ultimate goal is to calculate their volume in order to quantify their impact on tracer transport. As mentioned in the methodology section, it is difficult to calculate the eddy volume with a single ship section; moreover, this calculation depends on the criteria used to delimit the core.

In this section, 6 criteria are analysed together with the eddy volume calculated in this way: Thermohaline anomalies on isopycnal surfaces (see equations (1) and (2)), relative vorticity (equation (5)), Brunt Vaisala frequency (equation (4)), norm of the buoyancy 2D gradient (equation (3)), *EPV* anomaly (equation (9)) and the ratio $\frac{\Delta EPV_z}{EPV_x}$ (equation (10)). Depending on the data resolution and noise, some criteria cannot be applied.

Here three well-sampled AC ($N^\circ 1$, 7 & 26, denoted C^+ in table 3) have been selected for which the 6 criteria can be applied. Eddy $N^\circ 1$ (the surface AC sampled during EUREC4A-OA) and eddy $N^\circ 7$ (the surface AC sampled during Physindien 2011) have the finest horizontal resolution, so the uncertainties are small. Eddy $N^\circ 26$ (the subsurface AC sampled in the Lofoten Basin) has a sharp boundary; although its sampling is not optimal, its structure raises interesting questions. For clarity, only figures dealing with $N^\circ 26$ are shown.

Table 5. Maximum values for temperature and salinity anomalies on isopycnals (anomalies calculated with respect to the climatological mean). These values are reached in the eddy cores. If there is no clear maximum in an eddy core, the enclosed water is not different from the surrounding water; this is indicated by a dash: the eddy is then considered to be not materially coherent. The last column indicates its Material Coherence (MC). Note that the presence of the eddy centre in a vertical section is not necessary to assess the MC.

Num	Cruise	Type	$\max(\Delta T)$ [$^{\circ}C$]	$\max(\Delta S)$ [psu]	MC [yes/no]
1	EUREC4A-OA	AC	-0.86	-0.34	Yes
2	EUREC4A-OA	AC	-1.6	-0.64	Yes
3	EUREC4A-OA	AC	-0.65	-0.24	Yes
4	MSM60	C	0.87	0.18	Yes
5	MSM60	C	0.3	-0.05	Yes
6	MSM60	C	-	-	No
7	PHY11	AC	1.55	0.28	Yes
8	PHY11	AC	2.55	0.63	Yes
9	M124	C	0.53	-0.07	Yes
10	M124	AC	0.46	-0.05	Yes
11	M124	AC	0.52	-0.03	Yes
12	M124	AC	0.49	-0.04	Yes
13	M124	AC	0.49	-0.04	Yes
14	M124	AC	0.66	0.01	Yes
15	M124	AC	0.73	0.04	Yes
16	M124	AC	0.81	0.06	Yes
17	M124	AC	0.49	-0.04	Yes
18	MSM74	AC	0.67	-0.08	Yes
19	MSM74	C	-0.78	-0.27	Yes
20	MSM74	C	-1.09	-0.31	Yes
21	MSM74	C	-	-	No
22	MSM74	AC	-	-	No
23	m160	C	-	-	No
24	KB2017606	AC	1.34	-0.02	Yes
25	KB2017606	AC	0.54	-0.1	Yes
26	KB2017606	AC	1.12	-0.03	Yes
27	HM2016611	AC	0.43	-0.12	Yes
28	HM2016611	AC	1.09	-0.04	Yes

605 The methods presented are carefully followed. Figure 7 shows the vertical section
606 of the ship overlaid with closed contours defined by the criteria. For the sake of clarity,
607 the quantities used to draw the contours are calculated only in the vicinity of the core.
608 In reality, due to the noise in the data, these criteria can also detect other features not
609 related to the eddy core. In the background the quantity $\frac{\Delta EPV_z}{EPV_x}$ is plotted. The eddy
610 volume is insensitive to the threshold chosen for $\frac{\Delta EPV_z}{EPV_x}$ because its gradient is very pro-
611 nounced at the eddy boundary. The difference in the eddy volume when choosing lev-
612 els 10 or 30 is less than 3%. However, this threshold must be greater than 10 for EPV_x
613 to be negligible before ΔEPV_z . This criterion highlights the deep core of the eddy be-
614 tween $-650m$ and $-1050m$. Above this core, for $\sigma_0 \in [27.7; 27.8]kg/m^3$, the quantity

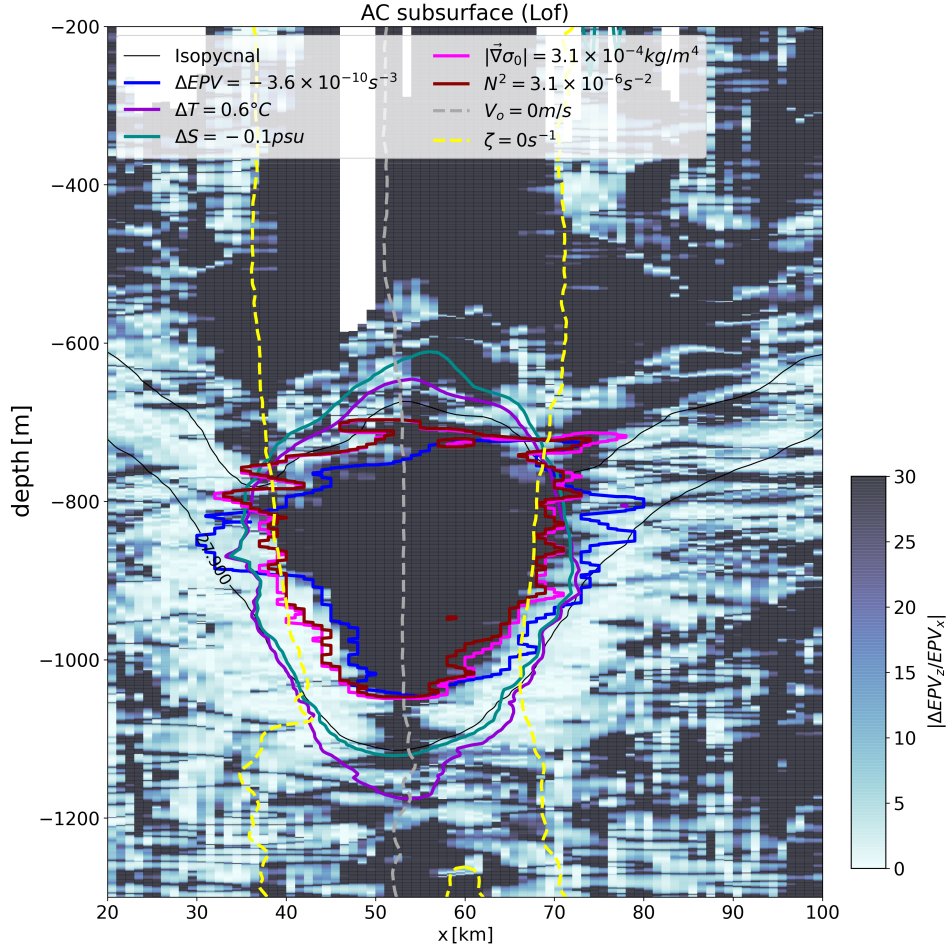


Figure 7. Outermost closed eddy contours calculated using 5 criteria: thermal anomalies on isopycnal surfaces in purple, salinity anomalies on isopycnal surfaces in green, relative vorticity in dashed yellow, Brunt-Väisälä frequency in brown, density gradient norm in pink, EPV anomaly in blue. The $\frac{\Delta EPV_z}{EPV_x} > 30$ criterion in the background, taken between the $\sigma_0 = 27.8 kg/m^3$ and $\sigma_0 = 27.9 kg/m^3$ surfaces, is also able to capture the core. The colour associated with this quantity has been saturated at level 30 to capture the region of weak frontality. The apparent eddy centre is shown as a dashed grey line, the isopycnals as thin dark lines. The eddy centre divides the core into two parts: the left (or right) side is used to determine the volumes using the ellipses (E_1) (or (E_2)).

615 $\frac{\Delta EPV_z}{EPV_x}$ decreases slightly: this marks the upper boundary of the core. Below this core,
 616 where $\sigma_0 > 27.88 kg/m^3$, the quantity $\frac{\Delta EPV_z}{EPV_x}$ decreases rapidly to values below 5, form-
 617 ing the lower eddy boundary. The lateral eddy boundary is characterised by $EPV_x \approx$
 618 ΔEPV_z , indicating that it is subject to symmetric instability.

619 This key finding is supported by the other five criteria. The region where $\frac{\Delta EPV_z}{EPV_x} >$
 620 30 is consistent with the region where: thermohaline anomalies reach an
 621 extremum; the core is quite homogeneous according to the density gradients and is as-
 622 sociated with a significant anomaly of potential vorticity. However, the relative vorticity
 623 seems to be less relevant for the detection of the upper and lower core boundaries.
 624 As this criterion only considers the velocity field, it does not distinguish materially co-

herent regions from others. As a consequence, the approximated volume appears much larger than that determined by the other criteria.

It is worth noting that the region where $\sigma_0 < 27.7\text{kg/m}^3$ is also characterised by the $\frac{\Delta EPV_z}{EPV_x} > 30$ criterion, although the materially coherent core appears to lie below it. In fact, since EPV lies on buoyancy gradients, a non-materially coherent region can be highlighted by buoyancy gradients created by isopycnal deviations. This shallower region is also consistent with the region where $\zeta_z < 0$.

Which of these criteria is most effective in detecting the materially coherent core? Some criteria have already been studied by Barabinot et al. (2023). They showed that the eddy core is surrounded by a turbulent region subject to instabilities characterised by a value of $\frac{EPV_x}{EPV_z}$ close to 1. Consequently, the largest values of the ratio $\frac{\Delta EPV_z}{EPV_x}$ define the eddy core, which is less subject to instabilities and where the trapped water is less likely to be mixed and modified by the environment. By superimposing the thermal anomaly and the $\frac{\Delta EPV_z}{EPV_x}$ contours, we determine the materially coherent core, which should undergo little change in properties during the eddy drift.

In other words, to capture the true materially coherent core of an eddy, two specific criteria are required. First, thermohaline anomalies on isopycnal surfaces must be computed to detect the region where the trapped water is located. The outermost closed contour is used to highlight an approximate eddy region. However, since thermohaline anomalies only give a locally defined line, some of the water in this region may be escaping from the core due to instabilities. Therefore the $\frac{\Delta EPV_z}{EPV_x}$ criterion is used within the first region to remove the boundary region subject to instabilities. The last region is much more restrictive, but represents the stable confined water inside the core.

In practice, it is difficult to apply the $\frac{\Delta EPV_z}{EPV_x}$ criterion to in-situ data because it requires high resolution data and is quite sensitive to noise. We now show that this criterion can be approximated by other criteria that are easier to compute.

5.2.2 3D eddy reconstruction

In this section, methods for approximating eddy volumes are applied to the AC of Figure 7. The eddy shapes are discussed before the numerical aspects are presented.

Figure 8 shows the 3D reconstructions assuming circularity of the eddy at each geopotential level. Since the position of the centre does not vary with depth, the eddy is axisymmetric. The reconstructed volume associated with the thermal anomaly is the most convex of all shapes. The eddy shape using the relative vorticity criterion is almost cylindrical and its upper and lower boundaries cannot be clearly distinguished. On the contrary, any other criterion leads to an eddy radius that decreases near the upper and lower boundaries: the volume is closed. Using the criterion on the norm of the 2D density gradient gives a similar shape to the Brunt-Väisälä frequency criterion. Except for the relative vorticity criterion, the eddy core is top shaped. The criterion on $\frac{\Delta EPV_z}{EPV_x}$ leads to a more conical eddy than the criteria based on gradients.

Figure 9 shows the 3D reconstructions assuming the vortex core is elliptical at each geopotential level. For $N^\circ 1$ the eccentricity is set to 0.782, for $N^\circ 7$ the value of 0.780 is kept, and for $N^\circ 26$ the value of 0.792 is kept. This figure refers to the ellipses (E1) mentioned earlier: the left side of the core was used to construct the volume. Again, the relative vorticity criterion leads to a cylindrical vortex shape. For all other criteria the eddy base is thinner than for circular eddies (see figure 8). This is consistent with figure 7, where the eddy bottom radius is smaller on the left than on the right. As before, criteria based on the Brunt-Väisälä frequency or on the norm of the 2D density gradient give eddy shapes similar to those with the $\frac{\Delta EPV_z}{EPV_x}$ criterion.

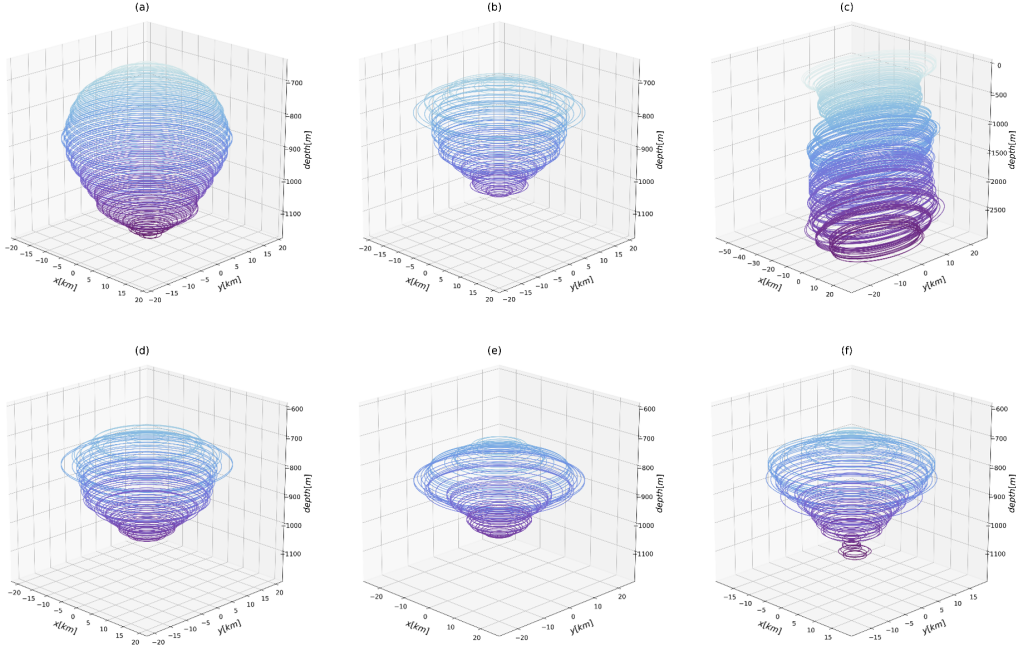


Figure 8. 3D reconstructions of AC $N^{\circ}26$ assuming its circularity at each geopotential level. Each panel corresponds to a criterion. The criteria are detailed in figure 7. (a): Thermal anomaly on isopycnals, (b): Brunt-Väisälä frequency, (c): relative vorticity, (d): norm of 2D density gradient, (e): Ertel potential vorticity anomaly, (f): $\frac{\Delta EPV_z}{EPV_x}$. Contours are plotted every five metres.

673 Figure 10 shows the 3D reconstructions again assuming the ellipticity of the eddy
 674 core at each geopotential level, this time using the right side of the core (ellipses E_2) to
 675 construct volumes. In this case the shapes are quite similar to those in figure 8, but the
 676 eddy volumes are larger. The thermal anomaly criterion results in a very convex shape.
 677 The Brunt-Väisälä frequency criterion and the 2D density gradient norm give shapes sim-
 678 ilar to those of the circular eddy. Except for the relative vorticity criterion, the bottom
 679 of each eddy is thinner than the top, similar to figure 8. We also recover the conical eddy
 680 using the criterion on $\frac{\Delta EPV_z}{EPV_x}$.

681 5.2.3 Comparison between eddy volumes

682 The volumes and uncertainties for the three eddies considered are now calculated
 683 and summarised in Figure 11. For each eddy, the volume has been normalised to the cylin-
 684 drical volume $\Omega_0 = \pi L^2 H$, where L and H are given in table 3 (note that L is defined
 685 in Figure 1). The normalised volumes for circular vortices are obviously closer to 1
 686 than for ellipses.

687 For any approximation method (circular or elliptical shape) the volume depends
 688 on the choice of criterion.

689 For example, for the eddy $N^{\circ}26$, assuming circularity, the volume is twice as small
 690 with the $\frac{\Delta EPV_z}{EPV_x}$ criterion than with the thermal anomaly criterion. Conversely, for a given
 691 criterion, the method based on ellipses gives larger volumes than the circular approx-
 692 imation. As expected, the relative vorticity criterion overestimates the entrapped vol-
 693 ume. The criteria based on the Brunt-Väisälä frequency, the norm of the 2D density gra-
 694 dient, the EPV anomaly and $\frac{\Delta EPV_z}{EPV_x}$ give closer values regardless of the method used.

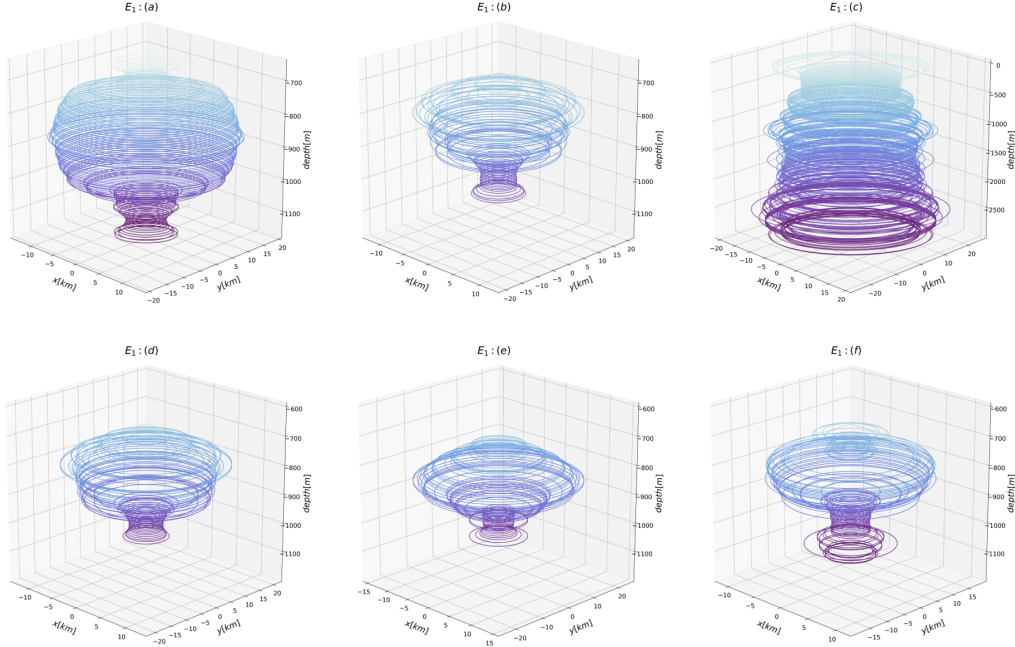


Figure 9. 3D reconstructions of AC $N^{\circ}26$ assuming the ellipticity of the eddy at each geopotential level. Each panel corresponds to one criterion. The criteria are detailed in figure 7. (a): Thermal anomaly on isopycnals, (b): Brunt-Väisälä frequency, (c): Relative vorticity, (d): 2D density gradient norm, (e): Ertel potential vorticity anomaly, (f): $\frac{\Delta EPV_z}{EPV_x}$. Contours are plotted every five metres.

695 In all cases, approximating the volume by a cylinder of constant radius with *in situ*
 696 data leads to an overestimation of the trapped volume. Conversely, for elliptical shapes
 697 the tracer transport is underestimated.

698 Using the $\frac{\Delta EPV_z}{EPV_x}$ criterion as a reference, relative differences with other criteria have
 699 been calculated and are shown in Figure 12. As mentioned above, thermohaline anom-
 700 alies on isopycnals lead to a larger volume estimate than with the $\frac{\Delta EPV_z}{EPV_x}$ criterion (see
 701 figure 7) and the relative difference between the volumes is large. For example, AC $N^{\circ}26$
 702 has twice the volume with thermohaline anomalies than with the $\frac{\Delta EPV_z}{EPV_x}$ criterion. The
 703 relative error between EPV anomaly and $\frac{\Delta EPV_z}{EPV_x}$ is also noticeable, reaching more than
 704 30% for eddy $N^{\circ}1$. Since the EPV anomaly is calculated using the horizontal contri-
 705 bution EPV_x , and since this term increases near the boundary, the total volume increases
 706 even as EPV_z decreases. Physically, the region where EPV_x is large is more likely to ex-
 707 perience frontal instabilities. Therefore, the water properties in this region can change
 708 due to mixing and the core can decay. As a consequence, the materially coherent core
 709 is somewhat overestimated by ΔEPV .

710 Finally, the most remarkable result is that the volume obtained with the N^2 cri-
 711 terion is a good approximation of that obtained with $\frac{\Delta EPV_z}{EPV_x}$. In fact, the relative error
 712 between the two computed volumes does not exceed 20%, whatever the eddy and what-
 713 ever the method used. The criterion-based norm of the 2D density gradient also gives
 714 similar results to the latter two, which is consistent with their mathematical definitions.
 715 In fact, eddies modify the local stratification due to their trapped water; this creates a
 716 baroclinic contribution to the buoyancy field. Consequently, the calculation of N^2 re-
 717 flects the eddy core.

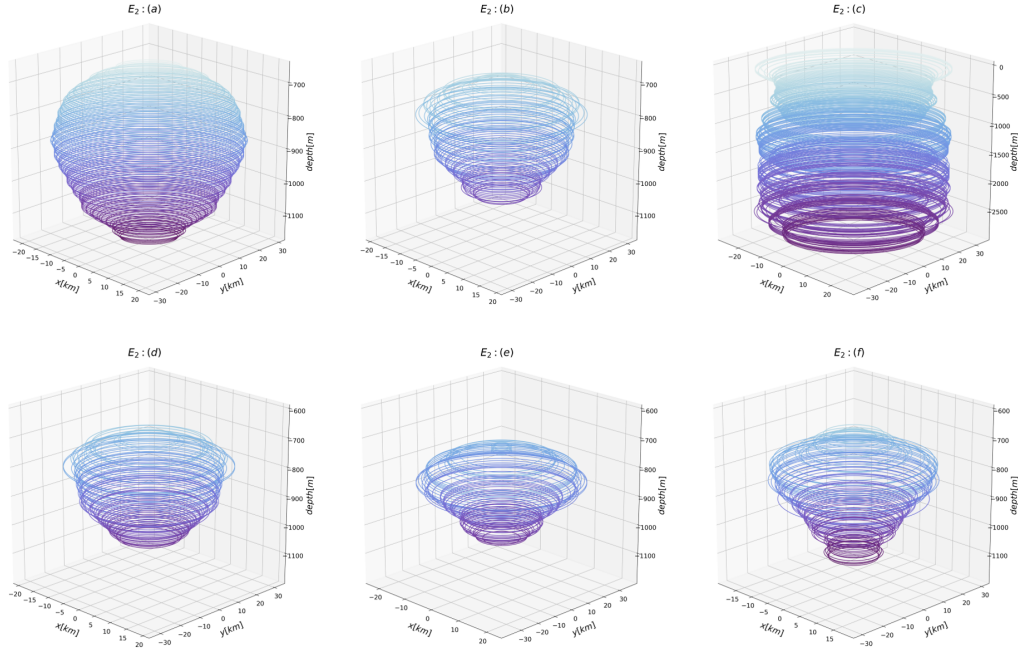


Figure 10. 3D reconstructions of AC $N^{\circ}26$ assuming its ellipticity at each geopotential level. Each panel corresponds to one criterion. The criteria are detailed in figure 7. (a): Thermal anomaly on isopycnals, (b): Brunt-Väisälä frequency, (c): Relative vorticity, (d): 2D density gradient norm, (e): Ertel potential vorticity anomaly, (f): $\frac{\Delta EPV_z}{EPV_x}$. Contours are plotted every five metres.

718 To illustrate this last point, Meunier et al. (2021) performed a decomposition of
 719 EPV into three terms for an eddy sampled by gliders in the Gulf of Mexico; they showed
 720 that eddy stretching (related to the vertical buoyancy gradient) was the dominant term.
 721 Our conclusions from Figure 12 are consistent with this result.

722 6 Conclusion

723 In this paper, we have evaluated the material coherence of mesoscale eddies using
 724 in situ data collected during several cruises (mostly in the Atlantic Ocean).

725 By analysing the relative errors, we show that the horizontal resolution of the hydrographic data (CTD, uCTD) and the vertical resolution of the velocity data are the most critical parameters for calculating the gradients of the physical quantities. Relative errors can reach 50% in the worst cases. Considering the mesoscale eddy size, future cruises should perform hydrographic measurements with a horizontal resolution finer than $10km$ and velocity measurements with vertical bins smaller than $8m$. It is also worth noting that very few cruises sampled eddy boundaries accurately and completely. This is an important feature to focus on in future cruises.

733 Despite the moderate resolution of our data and the small number of eddies considered, we have shown that materially coherent eddies are not the exception. Our main conclusions are that:

- 736 • materially coherent eddy cores are often located below the pycnocline and therefore cannot be detected as such using analyses based solely on satellite altimetry

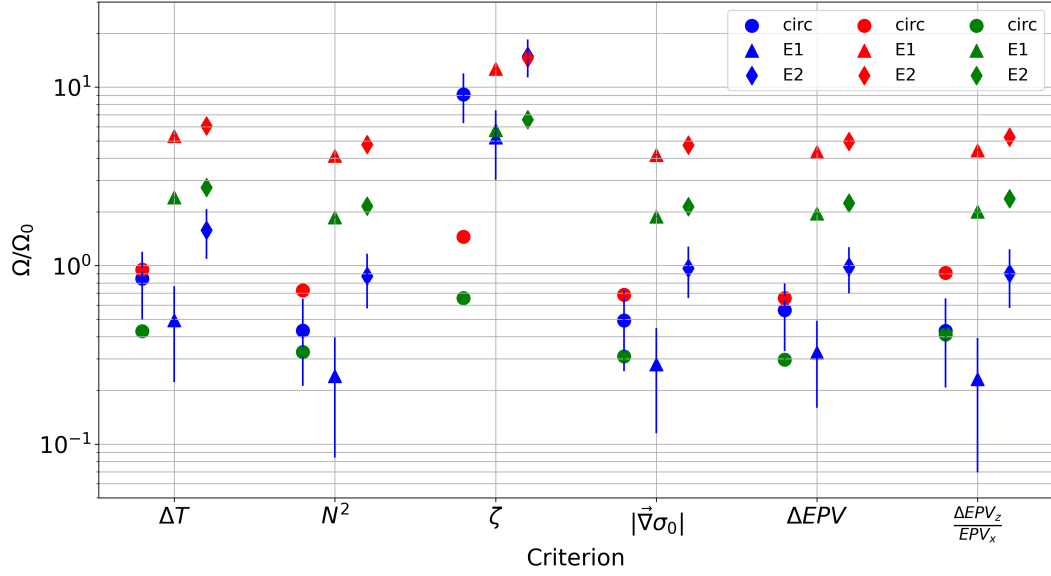


Figure 11. Normalised volume as a function of the criterion used, for eddies $N^\circ 1$ (green markers), $N^\circ 7$ (red markers), $N^\circ 26$ (blue markers) using the two reconstruction methods. Normalised volumes are plotted by criterion and by method. Error bars have been added but are only visible for AC $N^\circ 26$ because the horizontal resolution of AC $N^\circ 1$ and $N^\circ 7$ is finer than 3% of the apparent eddy radius L . Since the volumes obtained with the relative vorticity criterion are much larger than those obtained with other criteria, a logarithmic scale has been used.

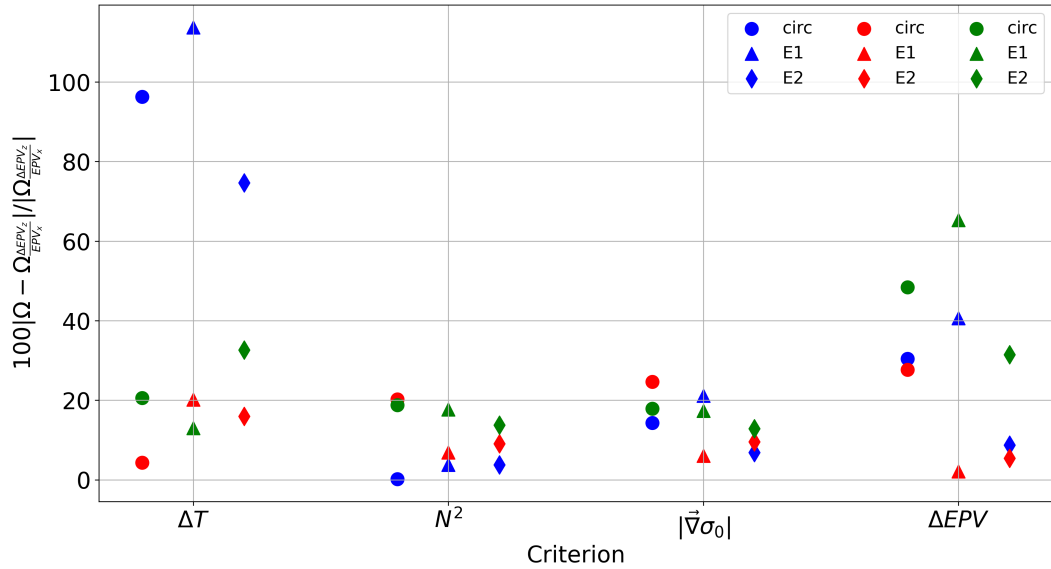


Figure 12. Relative gap between volumes approximations using that of $\frac{\Delta EPV_z}{EPV_x}$ as a reference. As in figure 11, results are plotted for eddies $N^\circ 1$ (green markers), $N^\circ 7$ (red markers), $N^\circ 26$ (blue markers)

are, the derived surface geostrophic velocity is not the appropriate velocity field to infer the material coherence of the eddy.

- A few eddies have been classified as surface intensified structures using velocity data. However, these eddies trapped their water mass much deeper. As a result, the use of surface fields alone is not sufficient to fully assess whether an eddy is materially coherent or not.
- These conclusions also hold for anticyclonic eddies. In our data set, cyclonic eddies were sampled at too low a resolution to make accurate analyses.
- A criterion developed by Barabinot et al. (2023) based on EPV characterises the eddy boundary, but indicates that it is subject to instabilities of small scales. Therefore, some of the water trapped by eddies and characterised by thermohaline anomalies may leak out of these eddies. Moreover, not only fluid particles can escape the core but also they can undergo some thermohaline changes at the eddy edge due to turbulent diffusion. Future studies should look at and quantify the permeability of eddies boundary in order to compute heat and salt volume lost during a time unite. This is not an easy task as it refers to meso and submeso scale processes.

We then proposed two methods to extrapolate the eddy volume using a single ship section. The first method assumes circularity of the eddy at each geopotential level and yields lower volumes than the second method, which assumes ellipticity of the eddy core. Volumes were also calculated and compared for different criteria. The outermost closed contour of the Brunt-Vaisala frequency is a good approximation for the materially coherent eddy core. This result confirms the conclusions of previous studies. This conclusion is also relevant for the study of eddies using ARGO profiler data.

Acknowledgments

This research has been supported by the European Union Horizon2020 research and innovation program under grant agreements no. 817578 (TRIATLAS), the Centre National d'Etudes Spatiales through the TOEddies and EUREC4A-OA projects, the French national programme LEFE INSU, IFREMER, the French vessel research fleet, the French research infrastructures AERIS and ODATIS, IPSL, the Chaire Chanel programme of the Geosciences Department at ENS, and the EUREC4A-OA JPI Ocean and Climate programme. We also warmly thank the captain and crew of RVs Atalante, Maria S. Merian and FS Meteor. Yan Barabinot is supported by a Ph.D grant from Ecole Normale Supérieure de Saclay. Xavier Carton acknowledges support by UBO and by a CNES contract EUREC4A-OA.

We benefited from numerous data sets freely available and listed here. Hydrographic and velocity data are freely available on the following links:

- EUREC⁴A-OA: RVs Atalante and Maria S Merian hydrographic data are freely available on the SEANOE website: <https://www.seanoe.org/data/00809/92071/>, accessed on 15 March 2021.
- METEOR 124: PANGAEA website, <https://doi.org/10.1594/PANGAEA.902947>, <https://doi.org/10.1594/PANGAEA.895426>, <https://doi.org/10.1594/PANGAEA.863017>, <https://doi.org/10.1594/PANGAEA.863015>, <https://doi.org/10.1594/PANGAEA.869740>
- PHYSIENDIEN 2011: Ifemer website, <https://co-en.ifremer.fr/eulerianPlatform?startDate=29%2F01%2F2014&>
- METEOR 160: PANGAEA website, <https://doi.org/10.1594/PANGAEA.943409>, <https://doi.org/10.1594/PANGAEA.943432>, <https://doi.org/10.1594/PANGAEA.943657>
- KB2017606 and HM2016611: NMDC website, <https://doi.org/10.21335/NMDC-1093031037>
- Maria S. Merian cruise MSM74: PANGAEA website, <https://www.pangaea.de/?q=campaign:name:%22MSM74>
- Maria S. Merian cruise MSM60: PANGAEA website, <https://www.pangaea.de/?q=campaign:name:%22MSM60>

References

788

789

790

791

792

793

794

795

796

797

798

799

800

801

802

803

804

805

806

807

808

809

810

811

812

813

814

815

816

817

818

819

820

821

822

823

824

825

826

827

828

829

830

831

832

833

834

835

836

837

838

839

840

841

- Barabinot, Y., Speich, S., & Carton, X. J. (2023). Defining mesoscale eddies boundaries from in-situ data and a theoretical framework. *Authorea*. doi: 10.22541/essoar.167870447.76933252/v1
- Bars, M. L., Aubert, O., Gal, P. L., & Marcus, P. S. (2011). Forme et persistance de tourbillons lenticulaires dans les écoulements stratifiés tournants : du laboratoire à la tâche rouge de jupiter !.
- Beron-Vera, F. J., Wang, Y., Olascoaga, M. J., Goñi, G., & Haller, G. (2013). Objective detection of oceanic eddies and the agulhas leakage. *Journal of Physical Oceanography*, *43*, 1426-1438.
- Bretherton, F. P. (1966). Critical layer instability in baroclinic flows. *Quarterly Journal of the Royal Meteorological Society*, *92*, 325-334.
- Carton, X. (2001). Hydrodynamical modeling of oceanic vortices. *Surveys in Geophysics*, *22*, 179-263.
- Carton, X., Flierl, G. R., Perrot, X., Meunier, T., & Sokolovskiy, M. A. (2010). Explosive instability of geostrophic vortices. part 1: baroclinic instability. *Theoretical and Computational Fluid Dynamics*, *24*, 125-130.
- Carton, X., & McWilliams, J. C. (1989). Barotropic and baroclinic instabilities of axisymmetric vortices in a quasigeostrophic model. *Elsevier oceanography series*, *50*, 225-244.
- Chaigneau, A., Eldin, G., & Dewitte, B. (2009). Eddy activity in the four major upwelling systems from satellite altimetry (1992-2007). *Progress in Oceanography*, *83*, 117-123.
- Chelton, D., Schlax, M. G., & Samelson, R. M. (2011). Global observations of nonlinear mesoscale eddies. *Progress in Oceanography*, *91*, 167-216.
- Chen, G., Han, G., & Yang, X. (2019). On the intrinsic shape of oceanic eddies derived from satellite altimetry. *Remote Sensing of Environment*.
- Chong, M. S., Perry, A. E., & Cantwell, B. J. (1990). A general classification of three-dimensional flow fields. *Physics of Fluids*, *2*, 765-777.
- Cushman-Roisin, B. (1994). Introduction to geophysical fluid dynamics.
- de Marez, C., Meunier, T., Morvan, M., L'Hégaret, P., & Carton, X. (2020). Study of the stability of a large realistic cyclonic eddy. *Ocean Modelling*.
- Dong, C., & McWilliams, J. C. (2007). A numerical study of island wakes in the southern california bight. *Continental Shelf Research*, *27*, 1233-1248.
- Dong, C., McWilliams, J. C., Liu, Y., & Chen, D. (2014). Global heat and salt transports by eddy movement. *Nature Communications*, *5*.
- Eliassen, A. (1951). Slow thermally or frictionally controlled meridional circulation in a circular vortex.
- Ertel, H. (1942). Ein neuer hydrodynamischer erhaltungssatz. *Naturwissenschaften*, *30*, 543-544.
- Fjørtoft, R. (1950). Application of integral theorems in deriving criteria of stability for laminar flow and for the baroclinic circular vortex. *Geofysiske Publikationer*, *17*, 1-52.
- Flierl, G. R. (1981). Particle motions in large-amplitude wave fields. *Geophysical and Astrophysical Fluid Dynamics*, *18*, 39-74.
- Gent, P. R., & McWilliams, J. C. (1986). The instability of barotropic circular vortices. *Geophysical and Astrophysical Fluid Dynamics*, *35*, 209-233.
- Hadjighasem, A., Farazmand, M., Blazeovski, D., Froyland, G., & Haller, G. (2017). A critical comparison of lagrangian methods for coherent structure detection. *Chaos*, *27* 5, 053104.
- Halle, C., & Pinkel, R. (2003). Internal wave variability in the beaufort sea during the winter of 1993/1994. *Journal of Geophysical Research*, *108*, 3210.
- Haller, G. (2000). Finding finite-time invariant manifolds in two-dimensional velocity fields. *Chaos*, *10* 1, 99-108.

- 842 Haller, G. (2005). An objective definition of a vortex. *Journal of Fluid Mechanics*,
843 525, 1 - 26.
- 844 Haller, G. (2015). Lagrangian coherent structures. *Annual Review of Fluid Mechan-*
845 *ics*, 47, 137-162.
- 846 Haller, G., Hadjighasem, A., Farazmand, M., & Huhn, F. (2015). Defining coherent
847 vortices objectively from the vorticity. *Journal of Fluid Mechanics*, 795, 136 -
848 173.
- 849 Hoskins, B. J. (1974). The role of potential vorticity in symmetric stability and in-
850 stability. *Quarterly Journal of the Royal Meteorological Society*, 100, 480-482.
- 851 Hunt, J. C. R., Wray, A. A., & Moin, P. (1988). Eddies, streams, and convergence
852 zones in turbulent flows.
- 853 Ioannou, A., Speich, S., & Laxenaire, R. (2022). Characterizing mesoscale eddies
854 of eastern upwelling origins in the atlantic ocean and their role in offshore
855 transport.
- 856 Joyce, T. M. (1977). A note on the lateral mixing of water masses. *Journal of Phys-*
857 *ical Oceanography*, 7, 626-629.
- 858 Joyce, T. M. (1984). Velocity and hydrographic structure of a gulf stream warm-core
859 ring. *Journal of Physical Oceanography*, 14, 936-947.
- 860 Laxenaire, R., Speich, S., Blanke, B., Chaigneau, A., Pegliasco, C., & Stegner, A.
861 (2018). Anticyclonic eddies connecting the western boundaries of indian and
862 atlantic oceans. *Journal of Geophysical Research: Oceans*.
- 863 Laxenaire, R., Speich, S., & Stegner, A. (2019). Evolution of the thermohaline struc-
864 ture of one agulhas ring reconstructed from satellite altimetry and argo floats.
865 *Journal of Geophysical Research*, 124, 8969-9003.
- 866 Laxenaire, R., Speich, S., & Stegner, A. (2020). Agulhas ring heat content and
867 transport in the south atlantic estimated by combining satellite altimetry and
868 argo profiling floats data. *Journal of Geophysical Research*, 125.
- 869 L'Hégaret, P., Carton, X., Louazel, S., & Boutin, G. (2015). Mesoscale eddies and
870 submesoscale structures of persian gulf water off the omani coast in spring
871 2011. *Ocean Science*, 12, 687-701.
- 872 Liu, T., Abernathey, R. P., Sinha, A., & Chen, D. (2019). Quantifying eulerian eddy
873 leakiness in an idealized model. *Journal of Geophysical Research*, 124, 8869-
874 8886.
- 875 Marshall, D. P., Maddison, J. R., & Berloff, P. (2012). A framework for param-
876 eterizing eddy potential vorticity fluxes. *Journal of Physical Oceanography*,
877 42, 539-557. Retrieved from [https://api.semanticscholar.org/CorpusID:
878 55840490](https://api.semanticscholar.org/CorpusID:55840490)
- 879 Marshall, D. P., Williams, R. G., & Lee, M.-M. (1999). The relation be-
880 tween eddy-induced transport and isopycnic gradients of potential vortic-
881 ity. *Journal of Physical Oceanography*, 29, 1571-1578. Retrieved from
882 <https://api.semanticscholar.org/CorpusID:131646498>
- 883 McWilliams, J. C. (1985). Submesoscale, coherent vortices in the ocean. *Reviews of*
884 *Geophysics*, 23, 165-182.
- 885 Meunier, T., Sanz, E. P., de Marez, C., Pérez, J., Tenreiro, M. F., Angulo, A. R., &
886 Bower, A. (2021). The dynamical structure of a warm core ring as inferred
887 from glider observations and along-track altimetry. *Remote. Sens.*, 13, 2456.
- 888 Nencioli, F., Kuwahara, V. S., Dickey, T. D., Rii, Y. M., & Bidigare, R. R. (2008).
889 Physical dynamics and biological implications of a mesoscale eddy in the lee of
890 hawai'i : Cyclone opal observations during e-flux iii. *Deep-sea Research Part*
891 *Ii-topical Studies in Oceanography*, 55, 1252-1274.
- 892 Pedlosky, J. (1964). The stability of currents in the atmosphere and the ocean: Part
893 i. *Journal of the Atmospheric Sciences*, 21, 201-219.
- 894 Pegliasco, C., Chaigneau, A., & Morrow, R. (2016). Spatio-temporal evolution of
895 two key processes impacting the observed vertical structure of the mesoscale
896 eddies in the 4 major eastern boundary upwelling systems.

- 897 Peliz, A., Boutov, D., Aguiar, A. C. B., & Carton, X. (2014). The gulf of cadiz gap
898 wind anticyclones. *Continental Shelf Research*, *91*, 171-191.
- 899 Pierre, L., Xavier, C., Stephanie, L., & Guillaume, B. (2016). Mesoscale eddies
900 and submesoscale structures of persian gulf water off the omani coast in
901 spring 2011. *Ocean Science*, *12*(3), 687-701. doi: [https://doi.org/10.5194/
902 os-12-687-2016](https://doi.org/10.5194/os-12-687-2016)
- 903 Ripa, P. (1991). General stability conditions for a multi-layer model. *Journal of
904 Fluid Mechanics*, *222*, 119 - 137.
- 905 Ruddick, B. R., Oakey, N. S., & Hebert, D. (2010). Measuring lateral heat flux
906 across a thermohaline front: A model and observational test. *Journal of Ma-
907 rine Research*, *68*, 523-539.
- 908 Rudnick, D. L. (2001). On the skewness of vorticity in the upper ocean. *Geophysical
909 Research Letters*, *28*.
- 910 Shcherbina, A. Y., D'Asaro, E. A., Lee, C. M., Klymak, J. M., Molemaker, M., &
911 McWilliams, J. C. (2013). Statistics of vertical vorticity, divergence, and strain
912 in a developed submesoscale turbulence field. *Geophysical Research Letters*,
913 *40*, 4706–4711.
- 914 Stammer, D. (1997). Global characteristics of ocean variability estimated from re-
915 gional topex/poseidon altimeter measurements. *Journal of Physical Oceanogra-
916 phy*, *27*, 1743-1769.
- 917 Tabor, M., & Klapper, I. (1994). Stretching and alignment in chaotic and turbulent
918 flows. *Chaos Solitons & Fractals*, *4*, 1031-1055.
- 919 Vortmeyer-Kley, R., Holtermann, P., Feudel, U., & Gräwe, U. (2019). Comparing
920 eulerian and lagrangian eddy census for a tide-less, semi-enclosed basin, the
921 baltic sea. *Ocean Dynamics*, *69*, 701-717.
- 922 Wang, Y., Olascoaga, M. J., & Beron-Vera, F. J. (2015). Coherent water transport
923 across the south atlantic. *Geophysical Research Letters*, *42*, 4072 - 4079.
- 924 Weiss, J. (1991). The dynamics of entropy transfer in two-dimensional hydrodynam-
925 ics. *Physica D: Nonlinear Phenomena*, *48*, 273-294.
- 926 Wunsch, C. (1999). Where do ocean eddy heat fluxes matter. *Journal of Geophysical
927 Research*, *104*, 13235-13249.
- 928 Xia, Q., Li, G., & Dong, C. (2022). Global oceanic mass transport by coherent ed-
929 dies. *Journal of Physical Oceanography*.
- 930 Zhang, Z., Tian, J., Qiu, B., Zhao, W., Chang, P., Wu, D., & Wan, X. (2016). Ob-
931 served 3d structure, generation, and dissipation of oceanic mesoscale eddies in
932 the south china sea. *Scientific Reports*, *6*.
- 933 Zhang, Z., Zhong, Y., Tian, J., Yang, Q., & Zhao, W. (2014). Estimation of eddy
934 heat transport in the global ocean from argo data. *Acta Oceanologica Sinica*,
935 *33*, 42-47.
- 936 Ōkubo, A. (1970). Horizontal dispersion of floatable particles in the vicinity of ve-
937 locity singularities such as convergences. *Deep Sea Research and Oceanographic
938 Abstracts*, *17*, 445-454.

Figure 1.

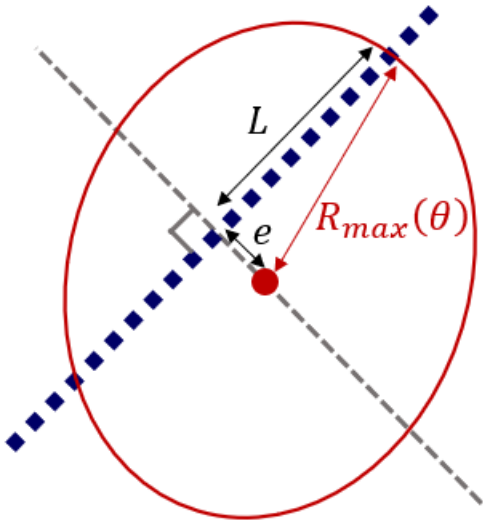


Figure 2.

Location of centers

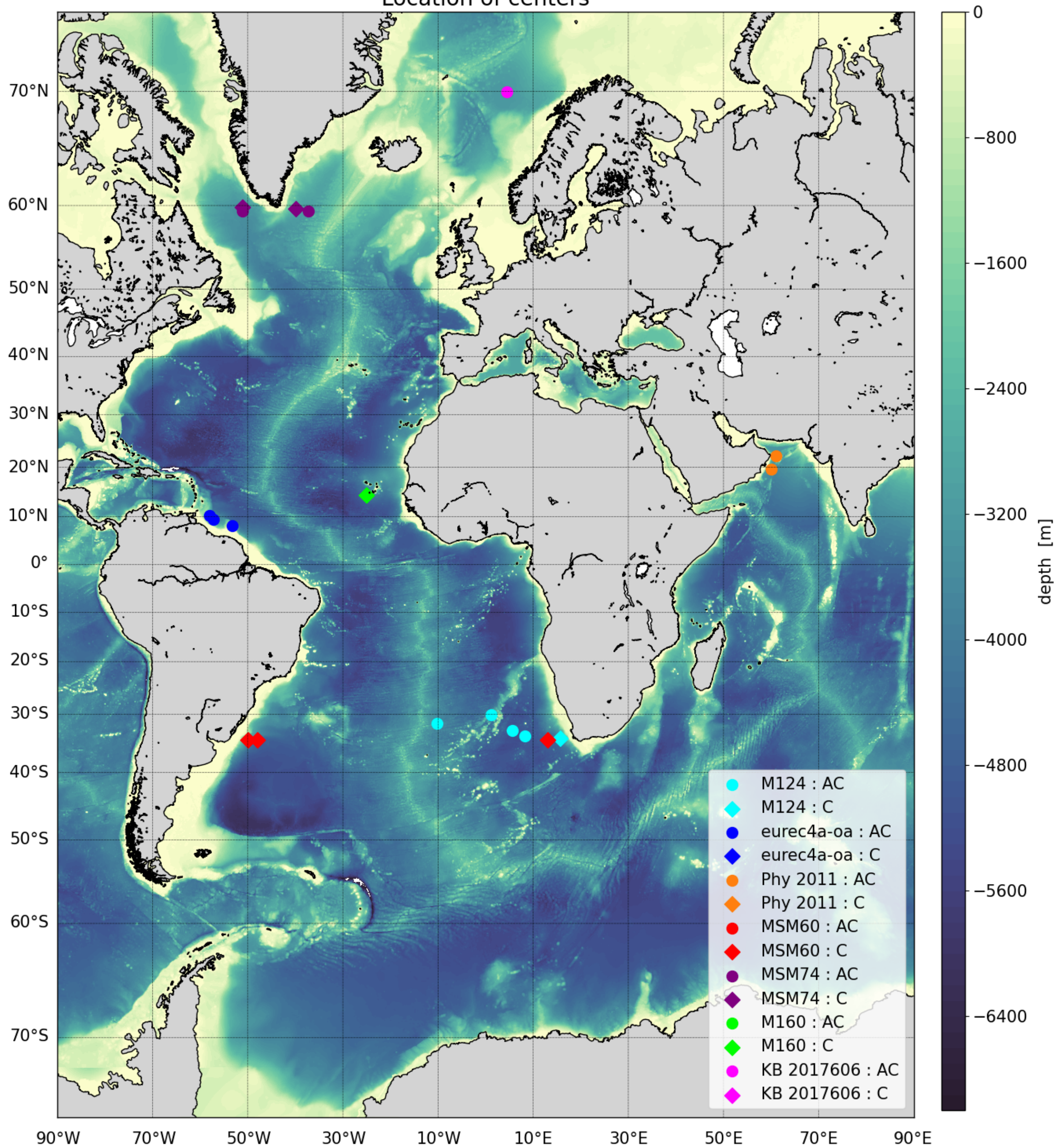


Figure 3.

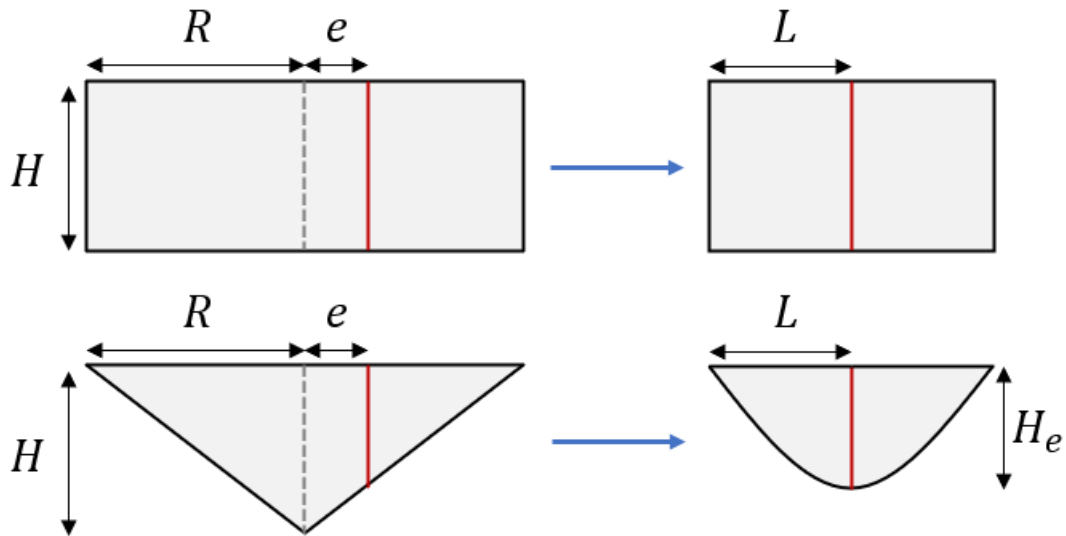


Figure 4.

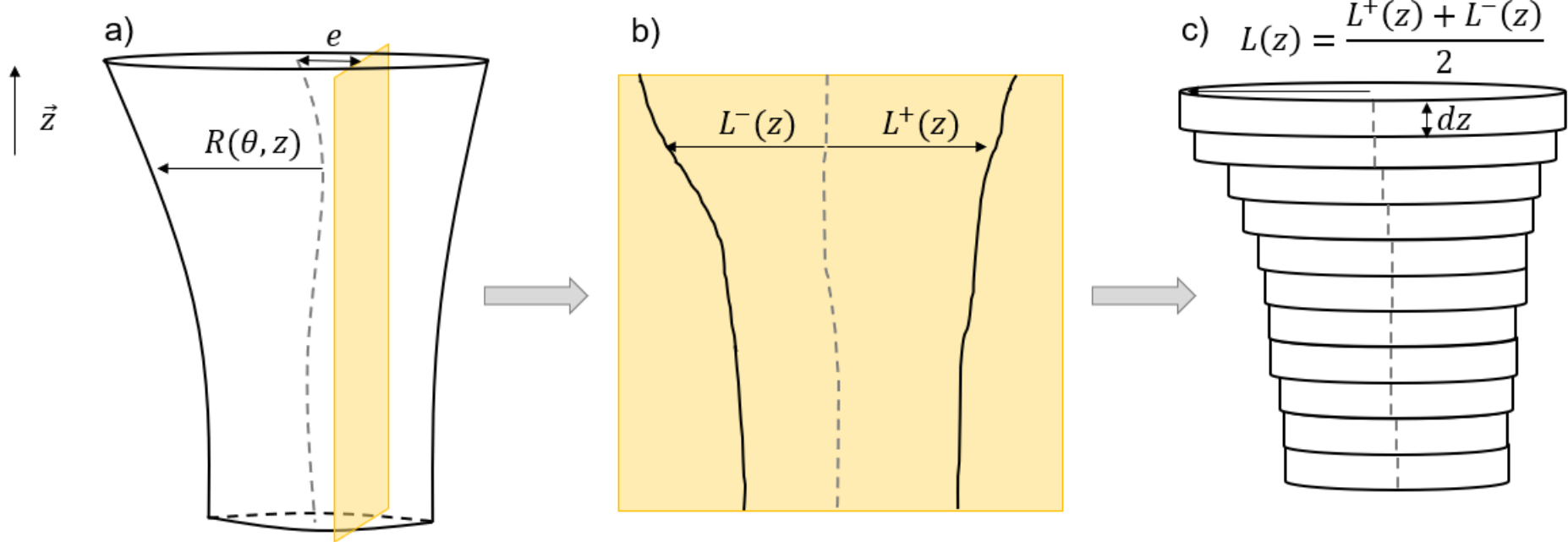


Figure 5.

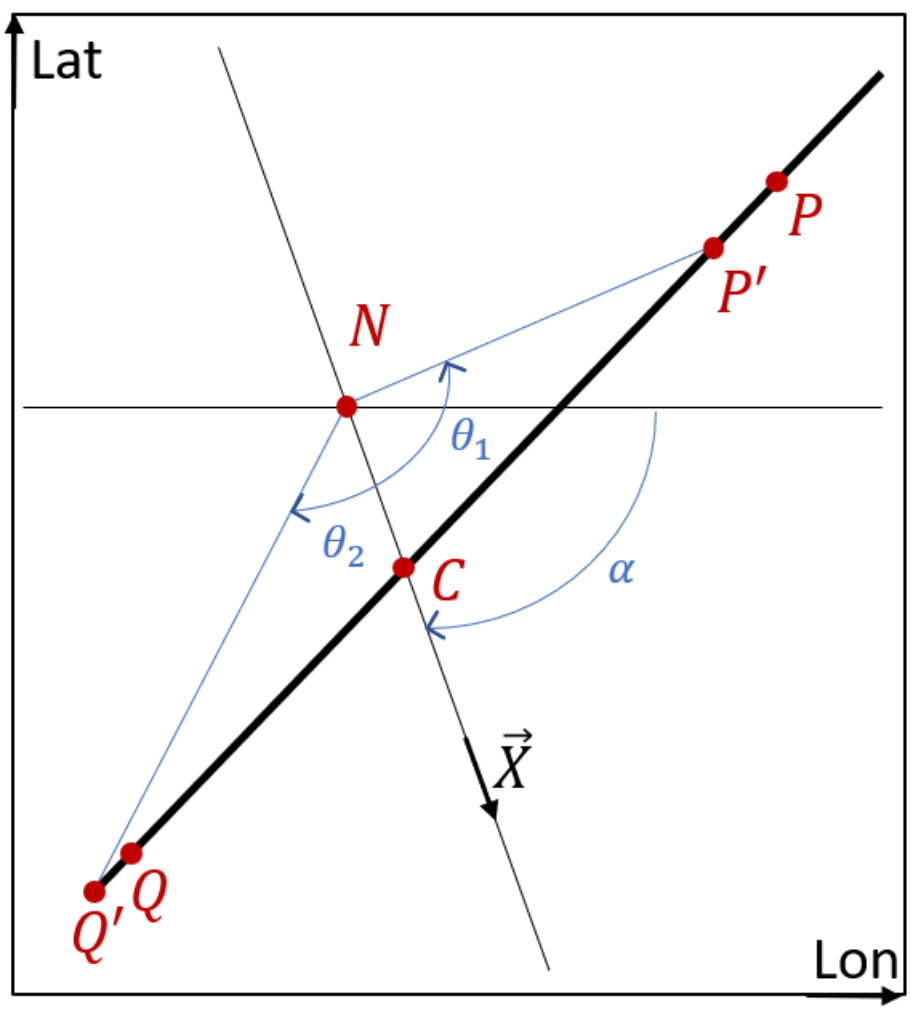


Figure 6.

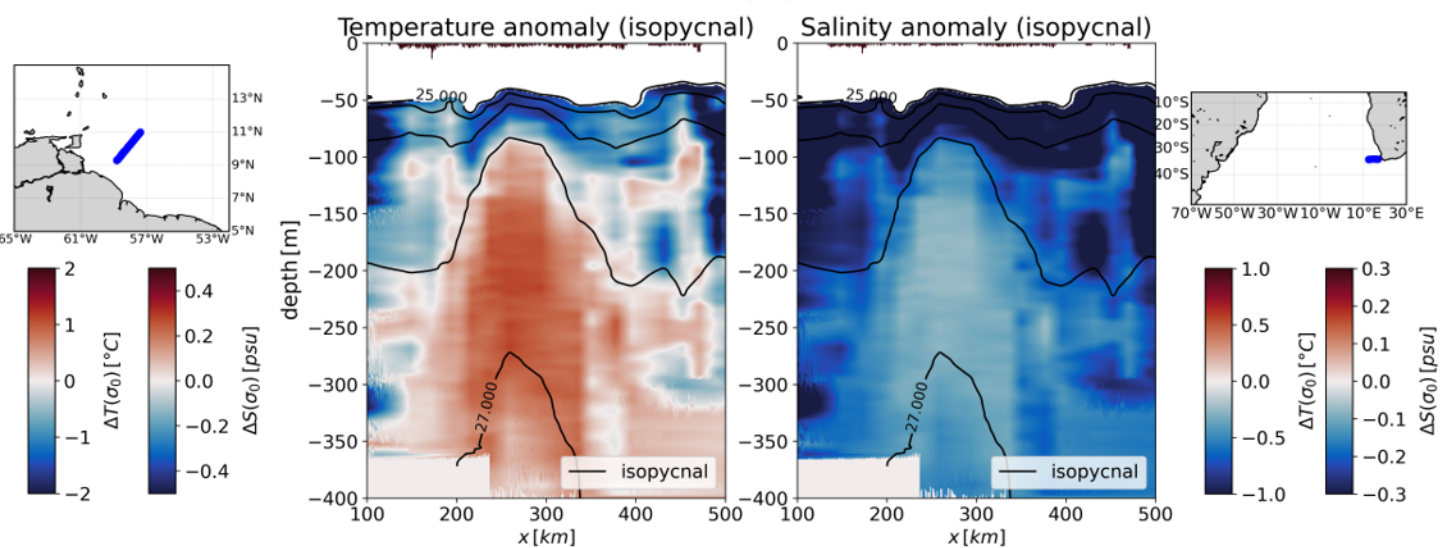
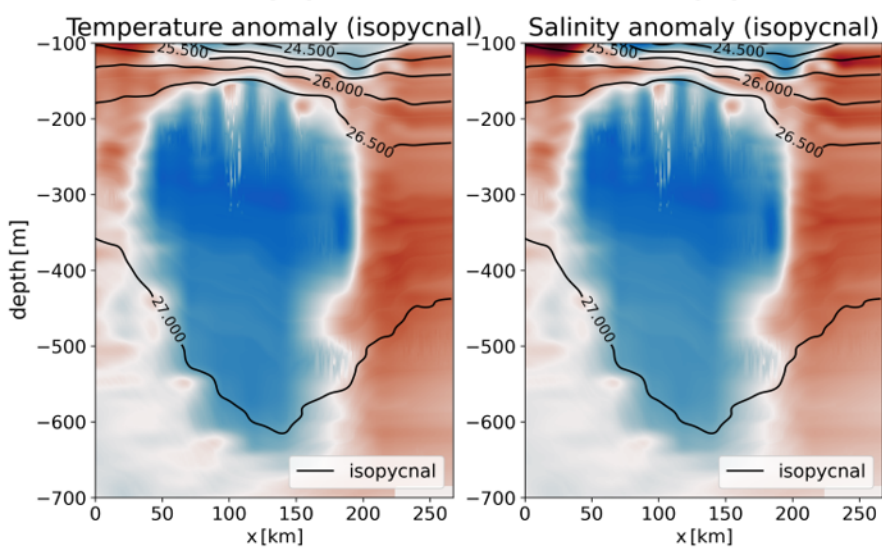
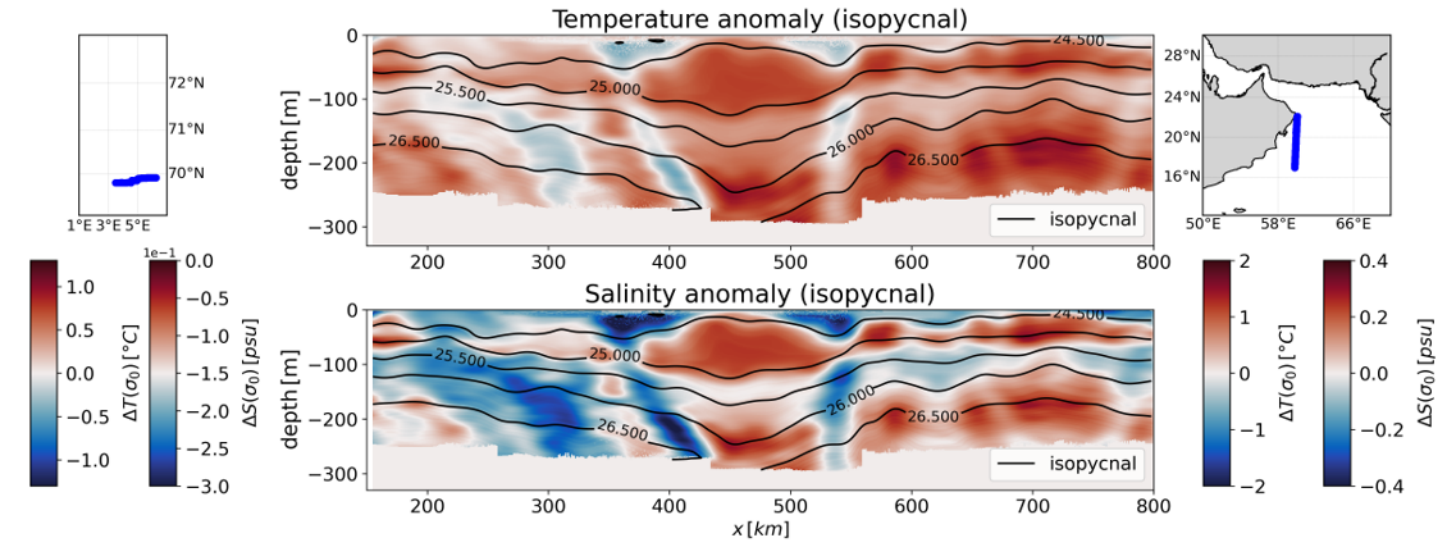
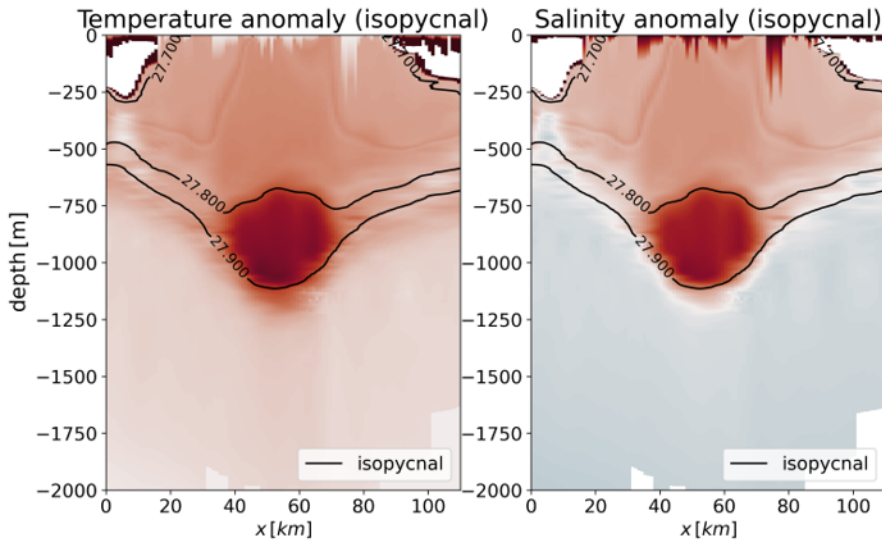


Figure 7.

AC subsurface (Lof)

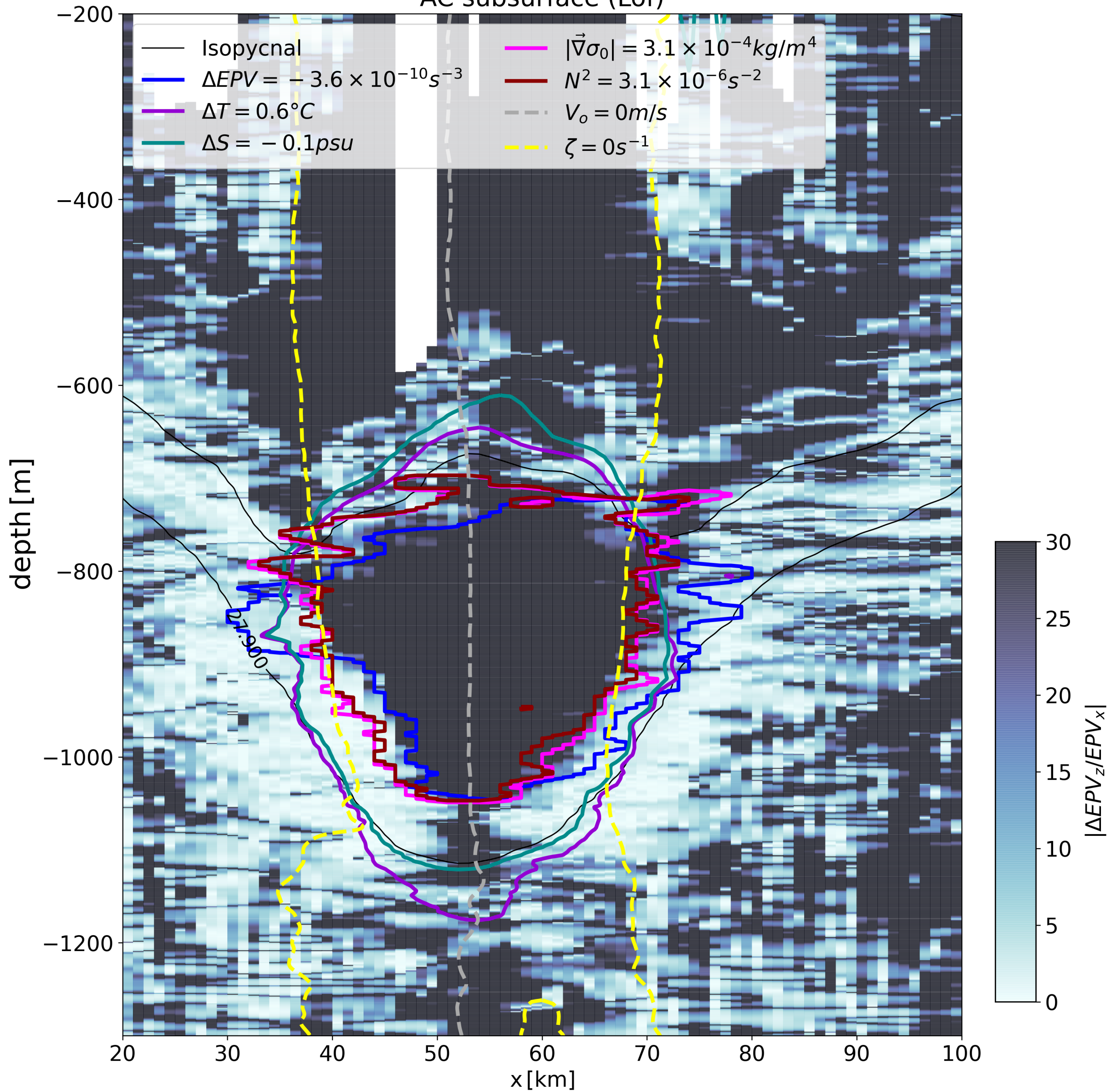
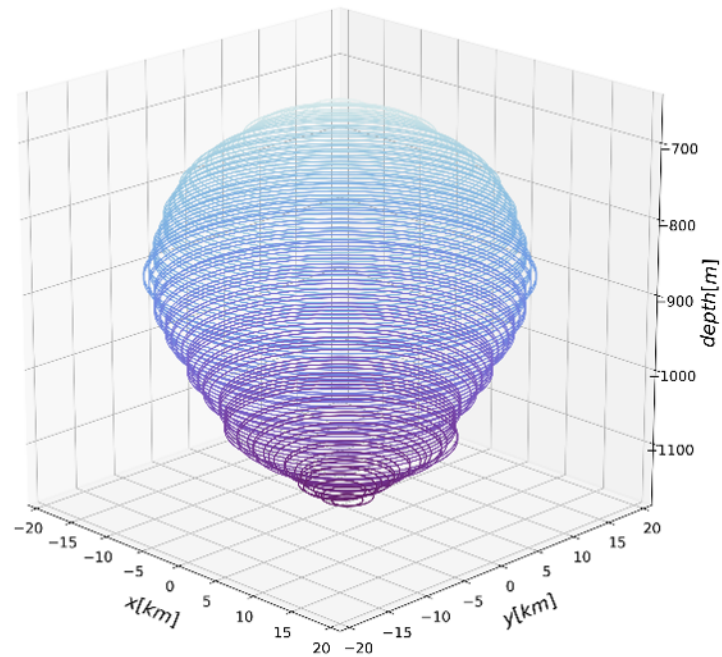
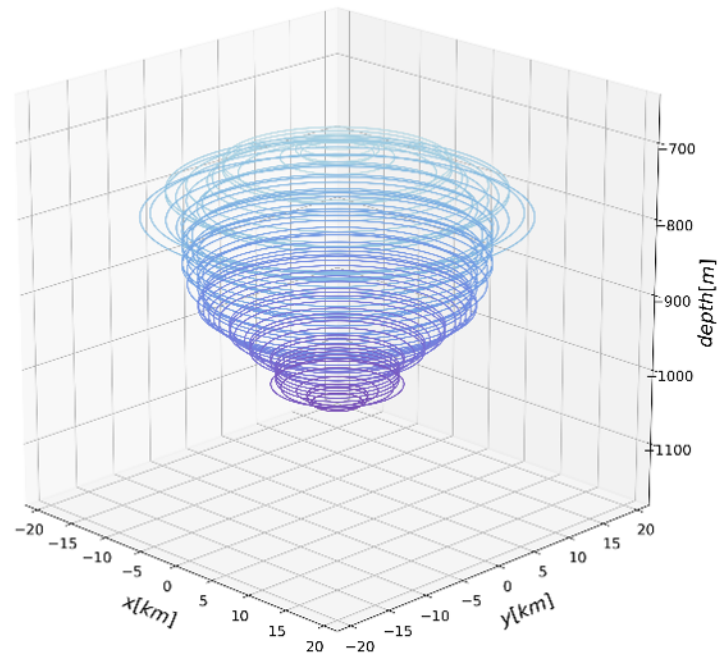


Figure 8.

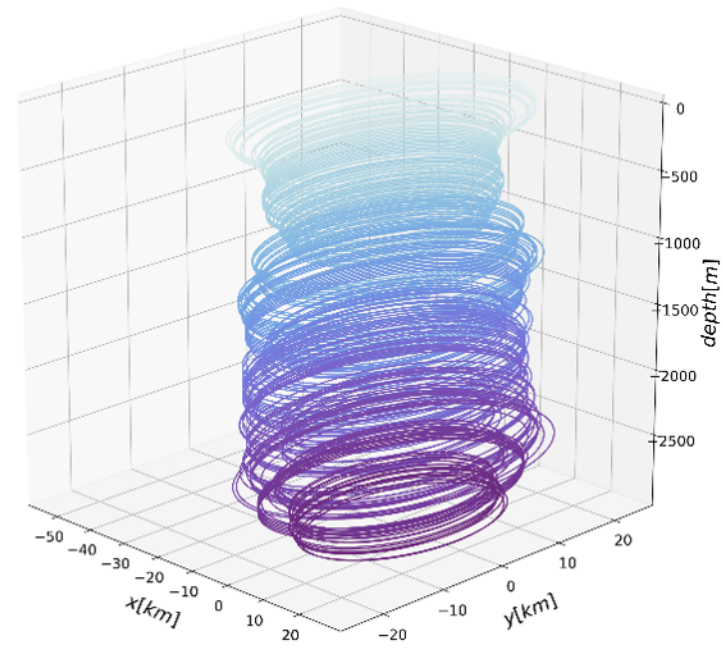
(a)



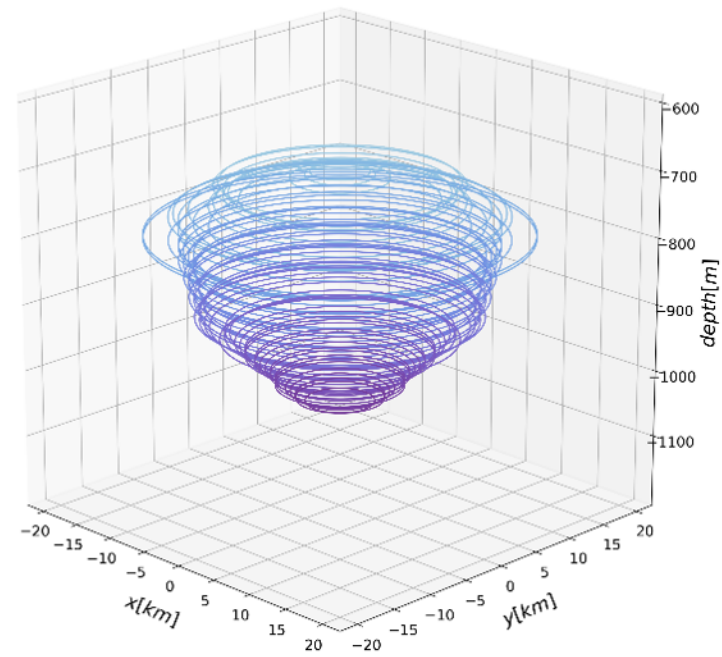
(b)



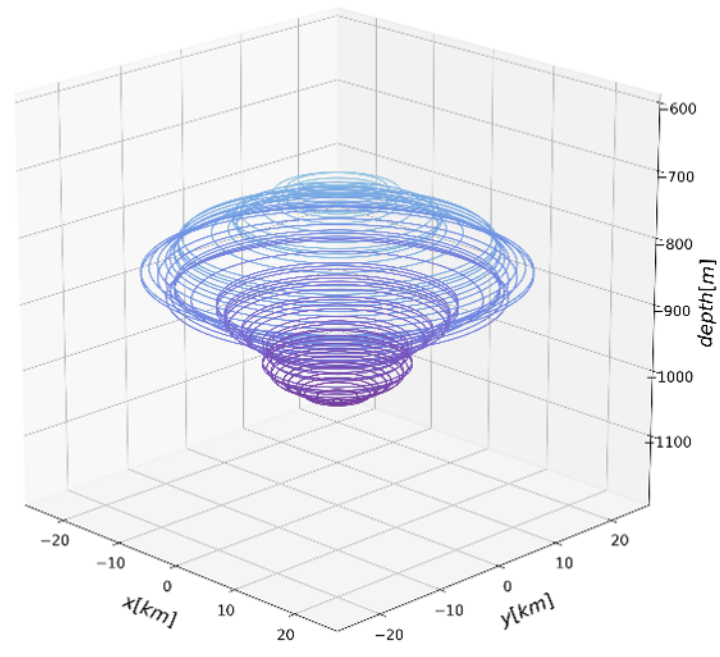
(c)



(d)



(e)



(f)

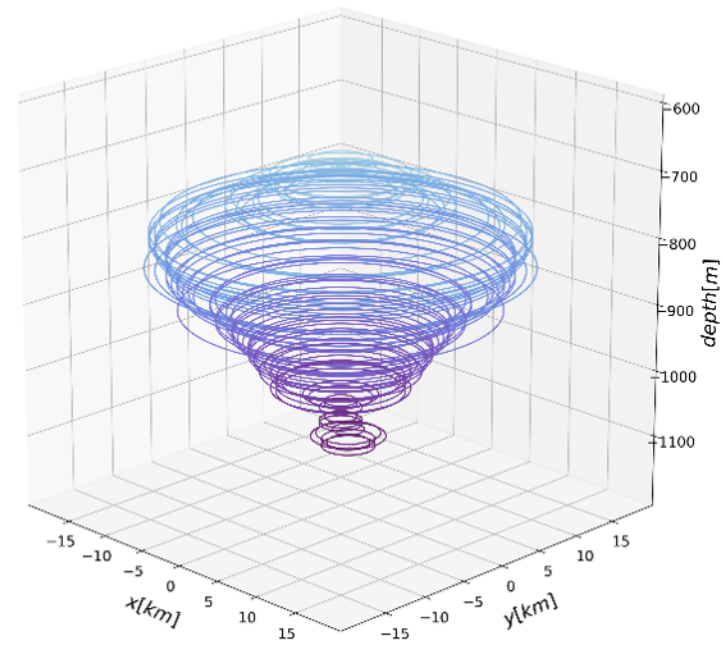


Figure 9.

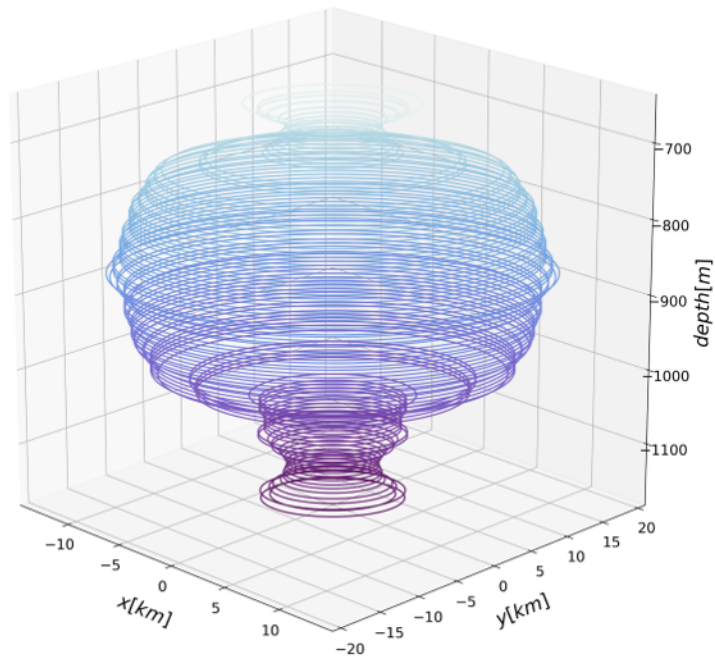
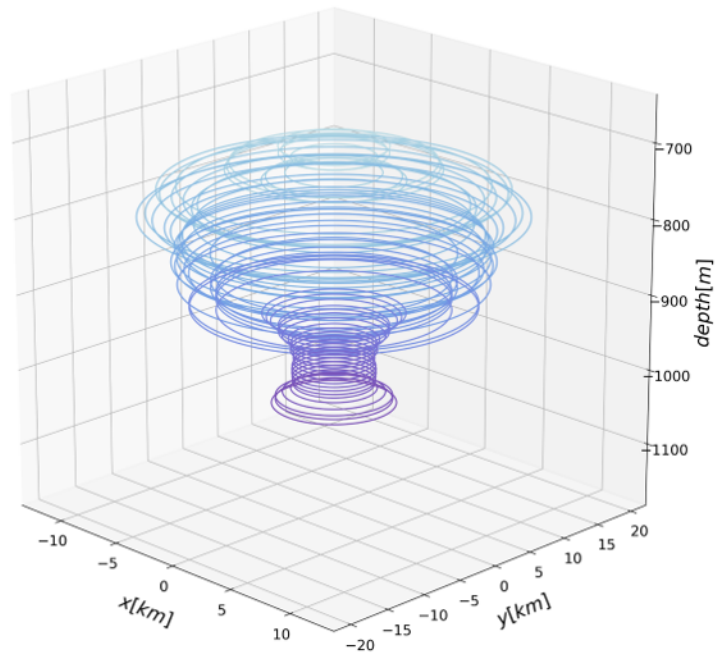
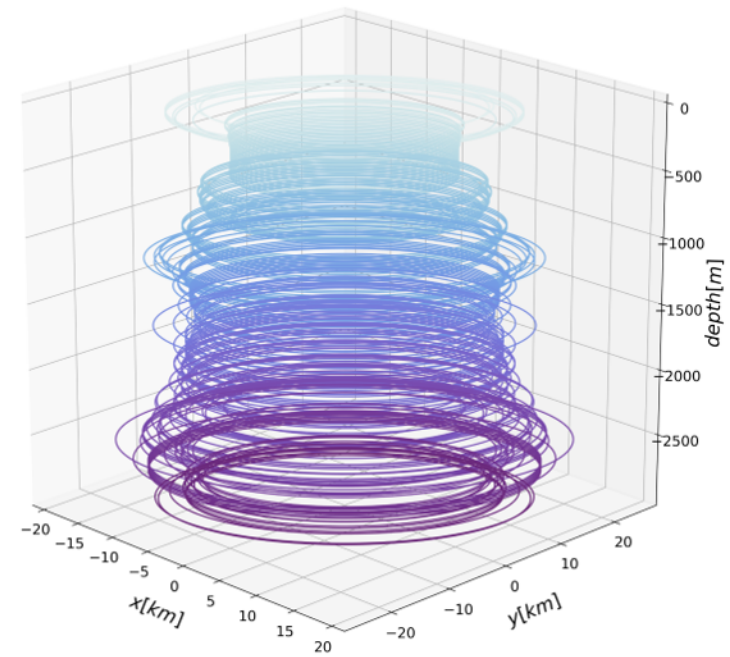
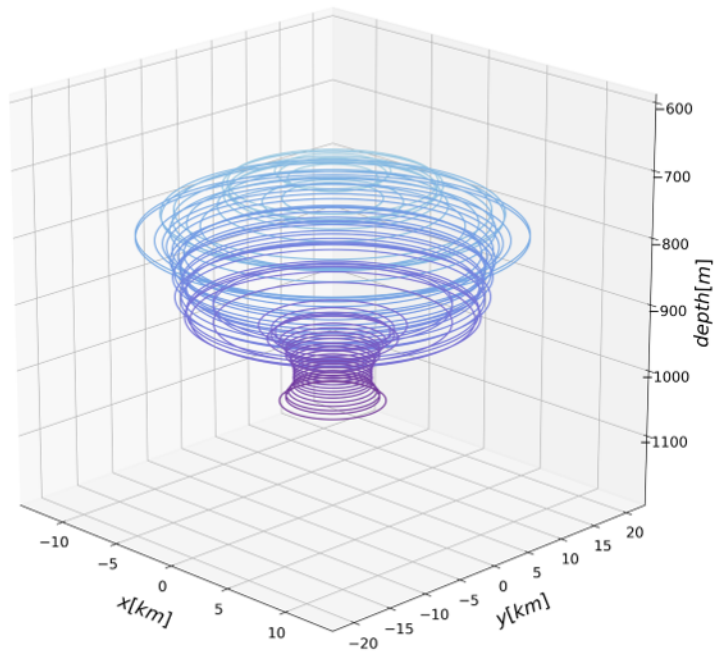
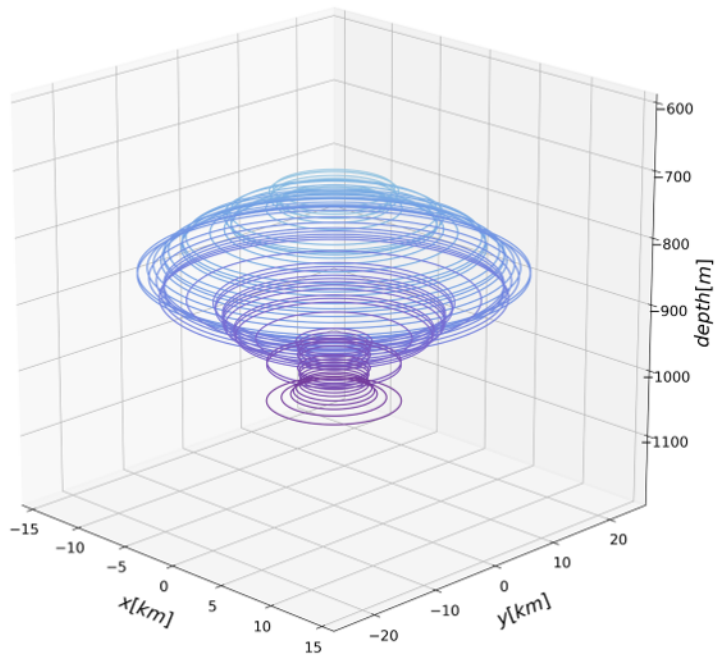
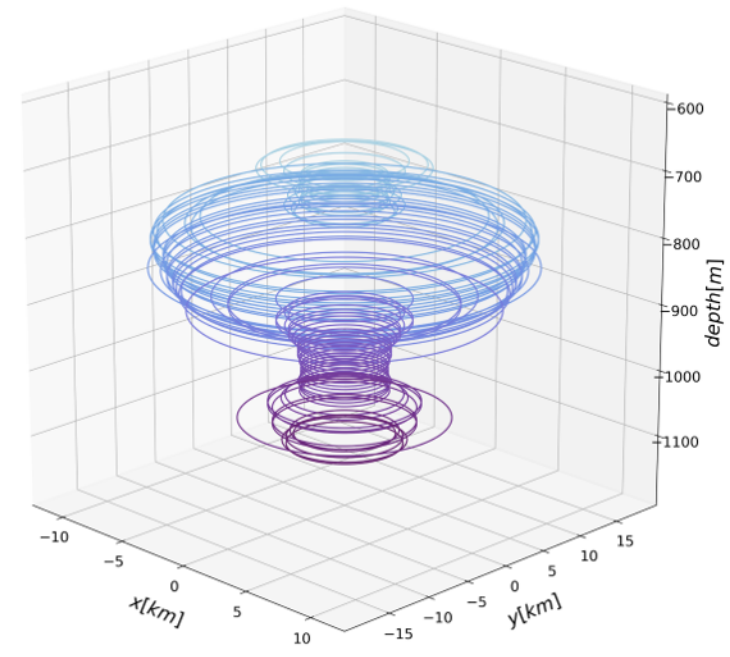
$E_1 : (a)$  $E_1 : (b)$  $E_1 : (c)$  $E_1 : (d)$  $E_1 : (e)$  $E_1 : (f)$ 

Figure 10.

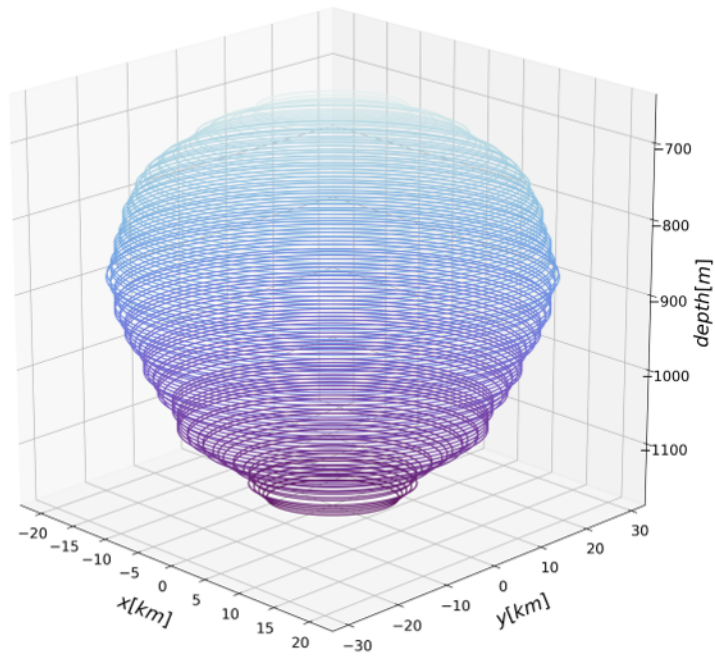
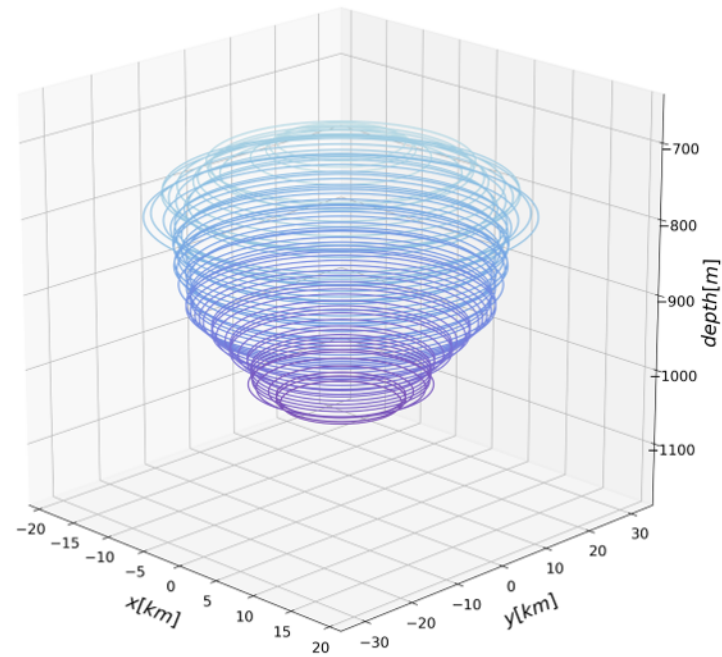
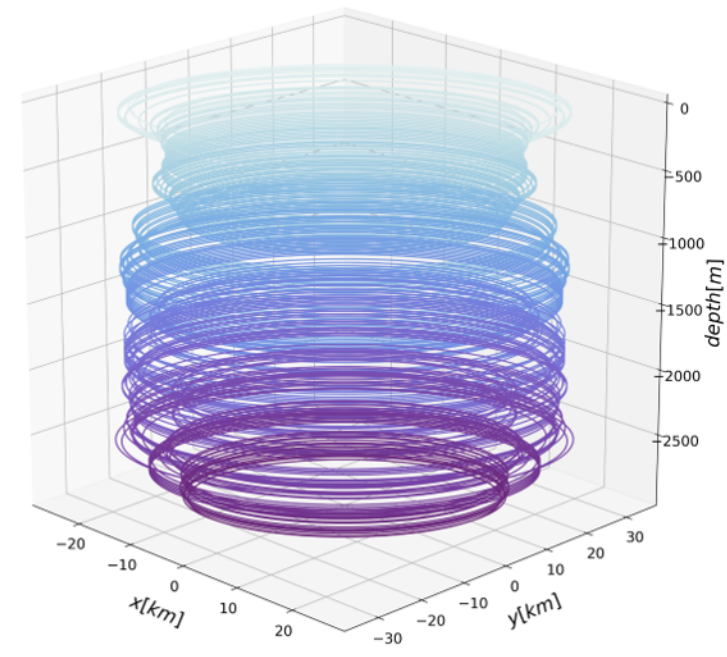
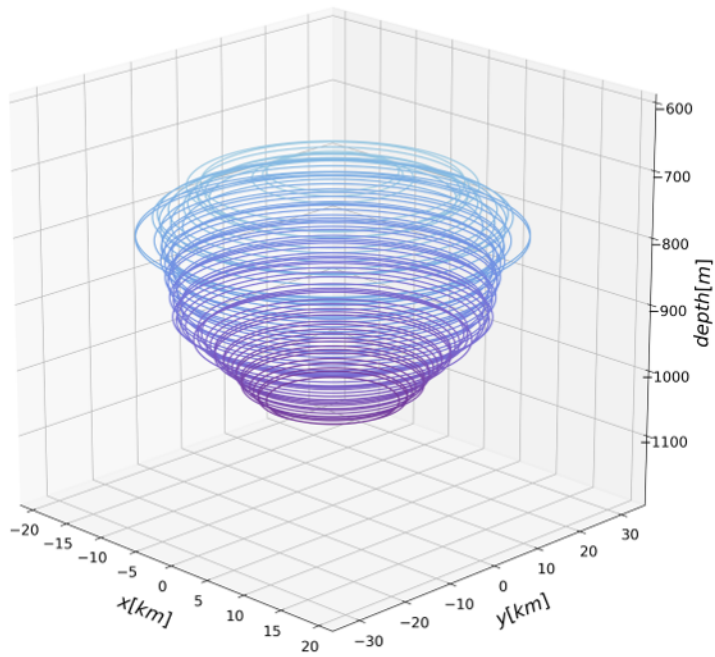
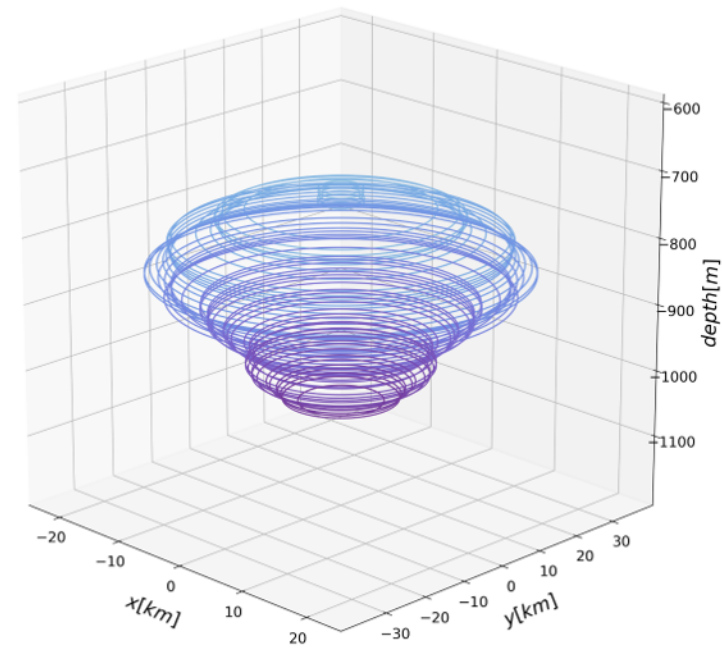
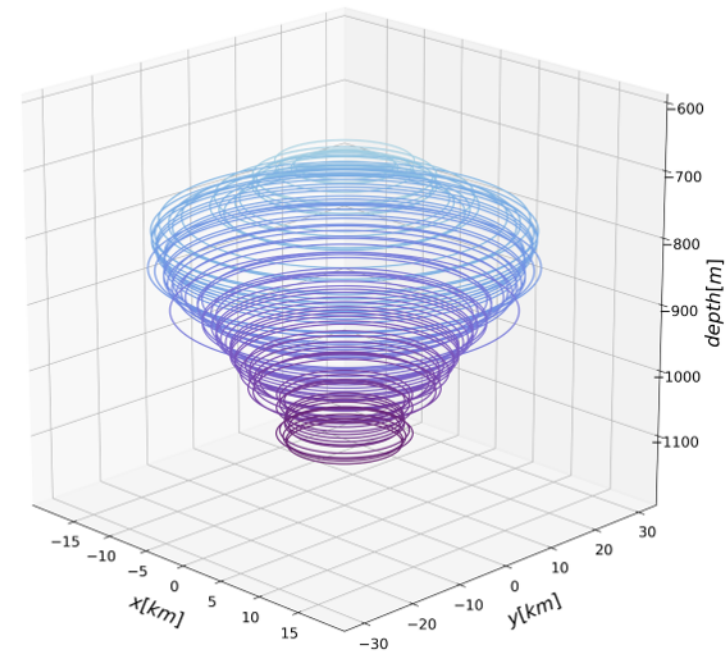
$E_2 : (a)$  $E_2 : (b)$  $E_2 : (c)$  $E_2 : (d)$  $E_2 : (e)$  $E_2 : (f)$ 

Figure 11.

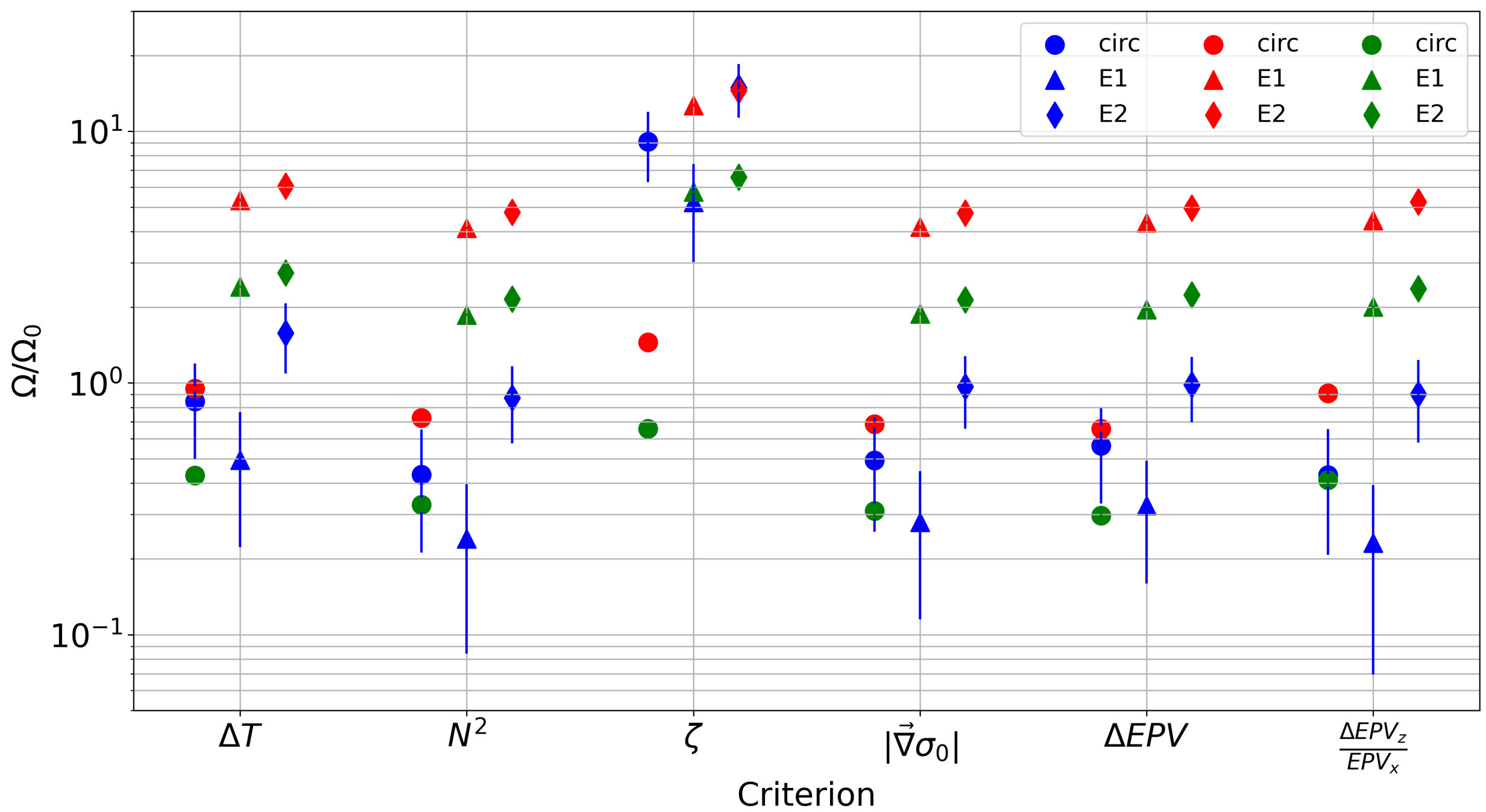


Figure 12.

